Master's thesis

NTNU
Norwegian University of Science and Technology
Faculty of Engineering
Department of Structural Engineering

Eirik Aas Kristiansen

Submerged floating tunnels in concrete exposed to blast loading

Master's thesis in Civil and Environmental Engineering
Supervisor: Tore Børvik, Martin Kristoffersen
March 2019

NTNU
Norwegian University of
Science and Technology

Eirik Aas Kristiansen

Submerged floating tunnels in concrete exposed to blast loading

Master's thesis in Civil and Environmental Engineering
Supervisor: Tore Børvik, Martin Kristoffersen
March 2019

Norwegian University of Science and Technology
Faculty of Engineering
Department of Structural Engineering

NTNU
Norwegian University of
Science and Technology

THIS PAGE INTENTIONALLY LEFT BLANK

Acknowledgments

This master thesis has been written in collaboration with the Structural Impact Laboratory (SIMLab) and the Department of Structural Engineering at the Norwegian University of Science and Technology during the spring/fall of 2018/-19.

Professor Tore Børvik and postdoc Martin Kristoffersen have supervised the thesis, offering crucial input and encouragement during the weekly follow-ups. I greatly appreciate them keeping their doors open for any questions throughout the entire thesis. Their guidance has been invaluable and is greatly appreciated, thank you.

Further thanks are extended to engineer at the Department of Structural Engineering, Trond Auestad, for carrying out the concrete material tests.

Finally my gratitude goes out to the Norwegian Public Roads Administration for making the study of such an interest subject a possibility.

Trondheim, March 4, 2019.

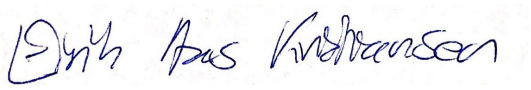

Eirik Aas Kristiansen

Abstract

A submerged floating tunnel(SFT) in has been proposed as a possible solution in crossing the Sognefjord as a part of the ferry-free E39 project. A potential safety hazard is an explosions inside the tunnel. Given that full-scale testing is highly impractical, numerical analyses coupled with scaled experiments is a good alternative.

Uniaxial compression and tensile splitting tests were conducted to determine the concrete properties and serve as a validation basis for the Karagozian and Case (K&C) material model. Digital image correlation was used to measure the specimen deformation, and showed promise in the pre-cracking regime, but failed to capture the behaviour after fracture. Subsequent numerical simulations of the material tests were done, and gave decent results. The K&C model is simple to use through its parameter generation only requiring input of compression strength, and tuning of the other parameters seems promising in improving its performance

The planned experimental testing on concrete pipes had to be adjusted during the thesis, and previously conducted test with internal blasts loads from C-4 charges was utilised for numerical comparison. Lagrangian simulations with the ConWep model underestimated the blast magnitude, but still overestimated the pipe damage. Nevertheless the results were qualitatively satisfying, and showed promise for further studies.

Table of Contents

Chapter 1

Introduction

The proposed solution of a submerged floating tunnel (SFT) crossing the Sognefjord is a part of the larger infrastructure undertaking: The E39 coastal highway route [1]. The project aims to connect the cities of Trondheim and Kristiansand by improving existing and constructing new roads, bridges, and tunnels. The total project has a projected total cost of around 40 billion USD, and should cut the current travel time of 21 hours in half. A major goal of the project is eliminating the need for ferries in crossing the numerous fjords. The depth and width of some of these fjords call for innovative solutions in designing and constructing the bridges and tunnels. In particular this is true for the crossing of the Sognefjord, with a depth of 1250 m and width of 3.7 km at the proposed crossing point. Due the large scale, a traditional suspension bridge is not viable. Among the considered options is an SFT. Possible design variations include connections to floating pontoons, or by tethering to the seabed. A feasibility study [2] confirmed the viability of the concept of the former, which is illustrated in figure 1.1.

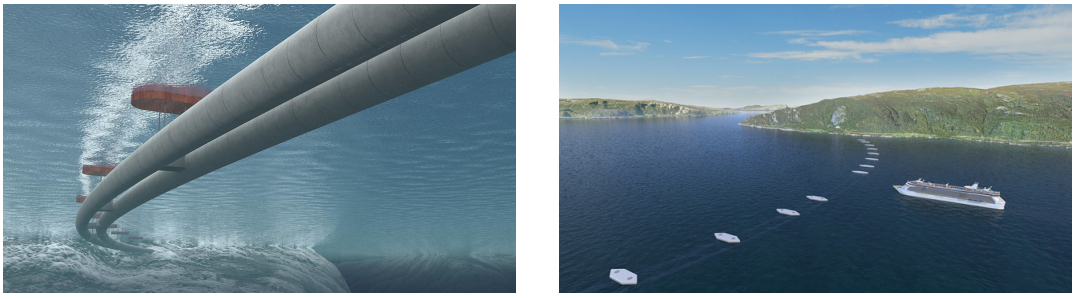

Figure 1.1: Concept illustration of an SFT crossing the Sognefjord. *Credit:The Norwegian Public Roads Administration.*

As per yet no submerged floating tunnels has been constructed. Among all the load scenarios to be considered, blast loading from explosions inside the tunnels potentially poses a major safety risk. The complexity of the SFT concept, along with the impracticality of full-scale testing, means numerical analyses offer a powerful tool in assessing

the structual behaviour. For such tools to be viable – in particular for the highly transient blast load scenario – a pivotal precondition is validated, capable material models.

This thesis aims to study the response of concrete when subjected to blast loads. Experimental test with digital image correlation, followed by numerical simulations, will be used to examine the concrete material and how well the numerical tools and material model are able to predict its behaviour. Finally this will be applied in confined blast load simulations of concrete pipes to review the ability to replicate experimental tests.

Chapter 2

Literature Review

In recent years a vast number of studies on the blast response of concrete has been conducted. Concrete is generally known to offer good blast resistance.

A number of studies are conducted on possible measures to increase the blast resistance of concrete. Increasing structure/wall thickness and increasing the reinforcement is clearly effective measures, however unfeasible after a certain limit. Addition of fibre reinforcement has also shown to be effective [3].For the case of tunnels, adding tunnel lining was studied by Chaudhary et.al [4], and was also seen to increase blast resistance. Tiwari et al. has studied blast loads on tunnels in soil. [5]. The blast response of concrete beams was studied by Li et. al [6], concrete slabs by Luccioni et al. [7] and columns by Park et. al [8].

The K&C concrete material model developed by Malwar et al.[9] will be used to model the concrete in this thesis, and has in recent years been studied by e.g Guo et al. [10] and Wu et al. [11].

The process of afterburning that occurs in explosions after the shock wave phase is thought to have significant effect on the structural response in confined environments by adding extra energy through the secondary combustion of detonation products. In the context of structural design the studies on the effect of afterburn is more limited.

Postdoc at the Norwegian University of Science and Technology (NTNU) and co-supervisor of this thesis, Martin Kristoffersen, has studied submerged floating tunnels subjected to internal blast loading extensively [12][13] [14][15]. Co-authoring these articles were also the supervisor of this thesis, professor Tore Børvik. Amongst work is concrete and reinforcement steel material testing, shock tube experiments on concrete slabs, concrete pipes exposed to blast loading, as well as numerical studies on all of the experimental work. Simulations of full SFT cross-sections on different geometries were conducted, and indicated that the circular cross-section is preferable to rectangular ones with regards to blast resistance.

2.1 Previous Master Theses

This thesis is a continuation of previous master theses on the same subject by Haug and Osnes [16], Hillestad and Pettersen [17], Krone [18] and Skaare [19]. In this section the conducted work and findings of these theses are summarised.

Thesis of Haug & Osnes (2015)

The thesis of Haug and Osnes focused on the blast response of concrete plates. Experimental work consisted of concrete material testing, followed by shock tube testing of five 50 mm concrete plates subjected to different pressure loadings. The concrete was classified B45 by the supplier. Compression and tensile splitting tests gave an average cylindrical compression strength of 54.9 MPa and an average tensile strentgh of 4.14 MPa. Results from the five shock tube experiments are summarised in table 2.1.

Table 2.1: Summary of shock tube tests, thesis of Haug and Osnes [16]

Plate #	Peak pressure (MPa)	Damage	Comments
1	7.40	Minor surface cracking	Some prior surface cracking from bolt fastening
2	11.99	Minor surface cracking	Membrane ruptured prematurely; two additional test on same plate were conducted
3	6.62	No visible damage	Pre-damaged by four 7.62 mm AP bullets
4	18.5	Complete failure: loaded plate section launched out of the frame	Pressure profile did not resemble a Friedlander curve
5	18.78	Large cracks resembling bending failure	

The experiments were studied further numerically in the finite element code IMPETUS Afea Solver, while certain selected experiments additionally were attempted recreated using LS-DYNA and/or Europlexus. The concrete was mainly modelled using the Holmquist-Johnson-Cook (HJC) model in IMPETUS, while two others, namely the Dynamic Plastic Damage Concrete (DPDC) and K&C Concrete Damage Model (CDM), were applied in Europlexus and LS-DYNA respectively for selected problems.

In the numerical studies the pressure loading was applied using a Friedlander curve fit of the pressures measured in the experiments. The authors found that the HJC model needed extensive tuning to accurately reproduce the experimental results. It gave a reasonable prediction of the pressure magnitude that caused collapse of the plate, as well as reproducing the crack formation for two of the experiments (plates number 4

and 5). However, the model in general overestimated the plate capacity and showed a more ductile behaviour of the concrete than observed in the experiments. A material parameter study showed that the results was not significantly influenced by changing the concrete tensile strength parameter. This conflicted with the assumption that the concrete capacity is highly dependent on the tensile strength for the load scenario. Haug and Osnes thus further suggested that the HJC model might not be ideal for the particular problem. Simulations using the K&C Concrete Damage Model were less extensive, but still showed potential. Crack formation were reproduced with decent accuracy, while the collapse load of the plate also here was overestimated. The model was further deemed promising, on account of it only requiring three input parameters (compared to five for the HJC model), and on the limited tuning needed to reproduce the experimental results.

The thesis additionally examined effects of Fluid Structure Interaction (FSI) using finite element software Europlexus with the DPDC model. The inclusion of FSI effects proved to significantly increase computational cost, as well as requiring comprehensive work to obtain a viable mode. The authors remarked that the model still couldn't represent the pressure measurements from the experiments. For FSI-effects to be significant, cracks would have to propagate though the plate-thickness to allow for air to escape and thus lower the pressure on the concrete. Thus the FSI model was found redundant for design-purposes of the particular problem, as the possible improvement in accuracy wouldn't warrant the increase in computational costs.

In conclusion, Haug and Osnes made suggestions for further research:

- Numerical simulations of concrete material tests to better validate material models
- More accurate model setup for numerical simulations, i.e. inclusion of bolts and bolt holes in clamping assembly, as well as studying concrete plates with reinforcement.
- Numerical simulations of plates with varying thicknesses and boundary conditions.
- Apply stochastic material models for the concrete.
- Compare the results of using the same material model in different finite element software.

Thesis of Hillestad & Pettersen (2016)

Hillestad and Pettersen continued on the work by Haug and Osnes. They studied the blast response of plain and reinforced 50 mm concrete plates by experimental studies in the shock tube at NTNU SIMLab. Furthermore, initial material tests were conducted on both the concrete and the reinforcement steel to determine material the material properties. The concrete used in the tests were classified as B20 by the producer. Compression and tensile splitting tests gave an average cylindrical compression strength of 39.62 MPa, average cube compression strength of 46.35 MPa, and an average tensile strength

of 3.50 MPa. Uniaxial tensile tests on the reinforcement steel estimated the yield stress to be 794 MPa. Shock tube experiments were subsequently carried out on two reinforced and two plain plates. None of the plates experienced failure or through-thickness cracks. The plate response was similar for plain and reinforced plates, but the latter experienced smaller maximum displacement. For the reinforced plates the crack formation also seemed to align with the reinforcement mesh in a more rectangular pattern than for the plain plates. The results are summarised in table 2.2. The test id character indicate reinforced (R) or plain (P) plates, while the number is the nominal driver pressure in the test.

Numerical simulations of the shock tube tests were done in finite element codes LS-DYNA and Abaqus. The Karagozian and Case Concrete Damage Model (K&C) and the Concrete Damage Plasticity Model (CDP) were applied in LS-DYNA and Abaqus respectively. Additionally, Hillestad and Pettersen attempted to recreate the inhomogeneity of the concrete by developing two stochastic methods for the material modelling. The first, dubbed the random element strength method, assigned a random strength to each finite element based on a normal distribution. The second, dubbed the mesoscale method, discretizes the finite elements to either represent the aggregate or the matrix of the concrete. The model thus recreates the intrinsic inhomogeneity of the material. The different elements were here both represented with the K&C model, but with different material parameters. In accordance with suggestions made by Haug and Osnes [16], the entire clamping assembly was included in the numerical models to better represent the experimental setup of the shock tube.

Table 2.2: Summart of shock tube tests, thesis of Hillestad and Pettersen [17]

Test	**Peak pressure*** **(MPa)**	**Damage**	**Comments**
P-41	12.05	Smaller surface cracks	
R-41	12.27	Smaller surface cracks	Crack pattern follows the reinforcement mesh
P-77	16.55	Surface cracks on the back. Long continuous crack along bolt holes at front surface	
R-77	17.27	Smaller surface cracks on the back. More cracks on the front	Crack pattern follows the reinforcement mesh

* Peak pressures from Friedlander curve fit

The authors remarked that both the K&C and CDP material models recreated the experimental crack formation with reasonable accuracy, while in general overestimating the total damage. The stochastic methods gave similar plate displacement as the other

material models, but showed promise in predicting even more erratic - and thus realistic - crack patterns. The random element strength method required calibration for each mesh, and was noted to be better suited for problems with regularized mesh. Inclusion of erosion criteria in the models improved the ability to assess damage, but gave a reduced plate capacity, below what was observed in the shock tube tests.

In conclusion, the authors made suggestions for further work on the subject:

- Investigate the effects of different erosion criteria.
- Conducting scaled blast load experiments on concrete tubes, and/or experiments on concrete components with contact charges.
- Include FSI effects.
- Include shear reinforcement steel in the numerical model.
- Further studies on the random element strength and mesoscale methods.

Thesis of Skaare (2018)

Skaare [19] studied the response of concrete tubes exposed to internal blast loading. The experimental studies consisted of concrete compression tests, followed by testing of precast concrete tubes of two different sizes loaded by detonation of centrically placed charges of C-4. The smaller tubes were of 1500 mm length and 200 mm inner diameter, while the larger tubes had a length of 2250 mm and an inner diameter of 400 mm. A total of 18 tests were done : 6 on the smaller unreinforced tubes, 6 on the unreinforced larger tubes, and 6 on the reinforced larger tubes. Pressure was measured at different locations in the pipe wall and outside the pipe openings along its longitudinal axis.The pipes were made of B60 concrete, and material tests gave an average cube compression strength of 79.81 MPa. Digital Image Correlation (DIC) tool eCorr was used to measure the cube deformation, and produced good results until the point of cracking.

The smaller pipes experienced through-thickness cracking and fragmentation starting at a charge size of 14g. For the large unreinforced pipes failure was observed at a charge size of 65g, causing two longitudinal through thickness cracks splitting the pipe in two. Increasing the charge size for both pipe sizes caused the pipes to fragment in increasingly smaller pieces, as well as launching the fragments further away. For the reinforced large pipes significant spalling and cracking started at a charge size of 300g. At 500g the pipe showed high amounts of damage, with larger fragments of concrete being blown away at the middle section, exposing the reinforcement and showing through-thickness cracks.

The numerical studies were carried out in finite element code Abaqus/Explicit, where concrete was modelled by the Concrete Damage Plasticity (CDP) model with parameters gathered from Jankowiak and Lodygowski[20] and the loading was simulated using the CONWEP model. The simulations of unreinforced pipes generally produced decent

results for both the small and large sizes. Some of the longitudinal cracks observed experimentally were recreated, but the included erosion criteria caused excessive damage localised at the middle section, where close to all elements were eroded. Pipe failure was also observed for lower charge sizes than in the physical tests, and the model was not able to fully capture the observed failure modes. For the pipes with reinforcement the results were overall satisfactory. While still failing to fully capture the full cracking patterns and failure modes, the reinforcement seemed to regularize the behaviour of the concrete by alleviating some of the higher concrete strains. Skaare noted that the CDP model showed potential, but required significant tuning The CONWEP model is useful for simple prediction of blast loading, but underestimated the pressures that were measured experimentally, especially at areas further from the charge location. Eulerian simulations were thus also conducted in Europlexus to compare the predicted pressure loading. This model gave a more complex, realistic pressure distribution, but also these simulations severely underestimated the peak pressure magnitude. This emphasised the complexity involved in internal blasts and showed the significance of including confinement effects to better predict the actual pressure loading. To this goal Skaare thus suggested conducting full FSI simulations in further studies. Further suggestions were also made:

- Include strain rate effects in concrete modelling.
- Conduct material tests on reinforcement steel.
- Explore other concrete models, including statistical methods as used by Hillestad and Pettersen .
- Apply a more advanced erosion criteria in the concrete material model.

Thesis of Krone (2018)
Krone [18] also studied concrete pipes subjected to internal and external blast loading. The thesis considered experiments of 16 pipes carried out previously by Kristoffersen et al. [13], as well as conducting tests on 18 new pipes.

Initial compression tests were done on remaining concrete cubes from Hillestad and Pettersen's thesis in order to validate the concrete material models. DIC was used to measure the deformation of the cubes, and showed great promise in the pre-cracking domain. By this method the crack formation was observable before they were at all visible to the eye. From these tests an average cube compression strength was found to be 72.51 MPa. Pipes of inner diameter 200 mm and 400 mm were subjected to detonation from C-4 charges placed centrically in the pipe cross-section, as well as from internal and external contact charges on the pipe wall. Among the large pipes tested were also some with reinforcement. The tests along with the results will be discussed further in chapter 6

In general the tests showed that internal blasts and blasts from contact charges significantly increased the damage. This was in accordance to expectations, where shorter

stand-off distance and confinement effect are thought to decrease the blast resistance. Furthermore Krone noted that increasing the wall thickness, as well as introducing steel reinforcement were effective measures to increase said resistance.

The numerical studies applied the CDP model in ABAQUS, as well as the K&C model in LS-DYNA to describe the concrete material. Additionally the mesoscale and random element strength methods developed by Hillestad and Pettersen [17] were applied for simulation of the material tests, along with a new method combining the two. Loading was applied through the ConWep model, as well as through various distributions based on calibration of the Friedlander equation to the experimental pressure profiles. After tuning both material models produced reasonable results. The K&C model requires less input and calibration, but showed nonphysical behaviour for the post-peak domain as the material reached full damage. The CDP model required either scaling based on previously validated parameters, or a calibration based on an extensive experimental dataset. It was also strongly dependent on the chosen mesh, and might thus be more suited to regularized simulations with standard geometries. The results from both models overestimated the damage on the pipes, even though the blast pressures through ConWep was lower than in the experiments. Thus the author remarked that the simulations could indicate that neither material model is well suited for concrete subjected to blast loads.

Based on the findings in the thesis Krone made suggestions for further work.

- Explore other concrete materia models, e.g Holmquist-Johnson-Cook.
- Explore alternatives to the JWL equation of state.
- Explore other software, e.g IMPETUS or Europlexus.
- Eventually conduct analyses on full SFT-sections. Requires further validation of blast and material models.

THIS PAGE INTENTIONALLY LEFT BLANK

Chapter 3

Theory

This chapter introduces the fundamental theory that the work in this thesis is built on.

3.1 Submerged Floating Tunnels

3.1.1 Ferry free E39

3.2 Blast Loading

The subject of blast loading is wide and complex. Here the most important effects and mechanisms will be presented in a bid to offer an overview and an introduction to the subject. This section is mostly based on the work of Aune et. al [21], with additional input from Krauthammer [22]. The interested reader is referred to these works for a deeper understanding of the subject of blast loading. Where other sources have been used, this will be stated.

3.2.1 Explosions

Explosions can be divided in three main categories, as they may be of physical, chemical, or nuclear origin. Further subsets include astronomical, electrical, dust, and vapour cloud explosions, but will not be further discussed in this thesis. Physical explosions can be e.g volcanic eruptions or disastrous failures of pressure vessels. Chemical explosions are caused by combustion of highly energetic materials. More specifically the fuel elements in the material are rapidly oxidised. Conventional explosives, e.g. TNT, cause chemical explosions. Nuclear explosions are caused by the extreme release of energy through the processes of fusion (joining of light atoms) or fission (splitting of heavy atoms). There are as mentioned several possible origins for explosions in an SFT. One such example could be a gas explosion caused by a collision of a tanker truck carrying flammable or explosive gas. In such cases the blast loading and structural response

would be different than from detonation of high explosives. For the remainder of this thesis however the focus is on the latter of the two, because most research on the area of blast loading considers HE as the origin.

Detonation and deflagration
Two different processes can be present in the combustion of explosive/energetic materials. The combustion of such materials can be seen as a detonation wave travelling through the material, releasing chemical energy as the combustion processes propagate outwards in the material. If the speed of this combustion wave in the explosive is lower than the speed of sound in the material, the process is called *deflagration* and is caused by low explosives (LE). *Detonations* on the other hands are caused by high explosives (HE), for which the speed of the detonation wave is higher than the speed of sound in the material. High explosives that combust through detonation are therefore naturally the most critical in terms of blast design. A rule of thumb is that detonation of high explosives instantly releases about one-third of the available chemical energy, while the remainder is released through a slower process called afterburn.

TNT Equivalency
In order to compare to different explosives they are often expressed in terms of their TNT equivalency. The TNT equivalency can be found by comparing the energy released from the explosions of TNT and of the given explosive.

$$TNT_{eq} = W_{exp}\frac{E_{exp}}{E_{TNT}} \tag{3.1}$$

Here W_{exp} is the weight of the given explosive, and E_exp and E_{TNT} are the energy quantities released as heat by detonation of the explosive and TNT respectively. For design purposes, another approach is often used. in which the TNT equivalency indicates the necessary amount of TNT (in kg), TNT_{eq}, to produce an explosion with the same blast parameters as 1 kg of a given explosive. The most important parameters are often peak overpressure and impulse, and the equivalency factor will differ depending on which blast parameter one wishes to emulate. Some suggested TNT equivalencies of typical explosives are given in table 3.1.

The previous experiments which will be further assessed in this thesis were carried out by the use of C-4. C-4 is a very stable, mouldable plastic explosive. It is seen as a secondary explosive, meaning that detonation requires initiation by a shock wave from a primary explosive, i.e. a detonator.

Blast Phenomena

An explosion causes a sudden release of a large amount of energy accompanied by a rapid volume expansion. This expansion compresses the surrounding air, turning it into a dense gas layer. The movement and expansion of this gas layer is the cause of the arising shock wave, and the expanding boundary of this shock wave is further known as the shock front.

Table 3.1: Suggested TNT mass equivalencies from literature [22] [21]

Explosive	Equivalent TNT mass factor	
	by peak pressure	by impulse
Composition B	1.11	0.98
Composition C-4	1.37	1.19
Composition C-3	1.08	1.01
HMX	1.02	1.03
PETN	1.27	1.11
RDX	1.14	1.09
Amatol	0.99	0.98
Tritonal	1.07	0.96
Nitroglycerine	1.48	-
ANFO	0.82	-

Classifications of shock waves are often done based on their propagation velocities. The classification can be expressed through the Mach number M.

$$M = \frac{u}{c}$$

Where u is the velocity of the source, and c is the speed of sound in the medium. A Mach number of 1 thus signifies a shock wave travelling at the speed of sound in the given medium. For dry air at sea level, with temperature 20 °C, the speed of sound is approximately 343 m/s [23]. Combustion processes are related to the Mach numbers: deflagration gives Mach numbers $M < 1$, not producing shock waves, while detonation does produce shock waves, with Mach numbers $M > 1$. As the detonation wave reaches the outer boundaries of the explosive, a shock wave propagates outwards, while a rarefaction wave is created, travelling inwards to the centre of the charge. As the rarefaction wave reaches the charge centre, it causes the flow to overexpand, giving rise to a secondary shock wave, significantly smaller in pressure magnitude than the incident shock wave.

The incident wave from an explosion propagates in all directions from the origin, and in practically an instant rises to the maximum incident overpressure. As the shock wave spreads, the pressure decays in with the cube of the distance travelled (given a spherical charge), and settles at the ambient pressure. As the pressure wave passes a negative phase occurs, often longer than the positive one, but with a much smaller pressure magnitude. This negative phase is caused by the overexpansion of the gas caused by its momentum. The underpressure works to reverse the air flow towards the explosion origin after the incident wave passes. The typical pressure-time history from an explosion is shown in figure 3.1.

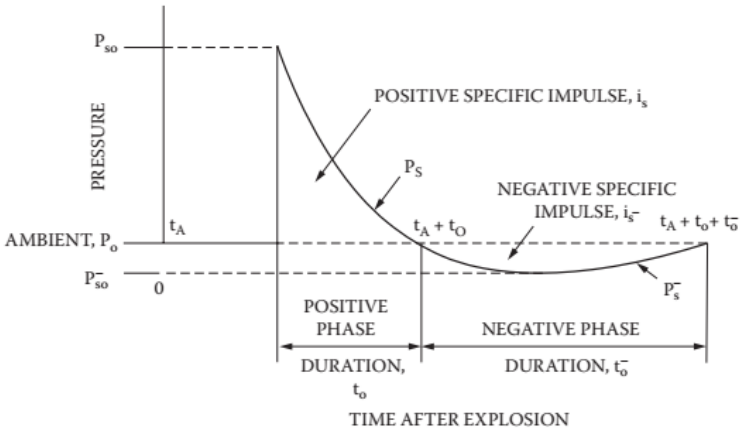

Figure 3.1: Typical pressure-time history of an ideal explosion shock wave. *Adapted from Krauthammer[22]*

Surface interaction

As the blast wave hits the ground, structure or other objects in it's path, a pressure loading is transferred to the given surface. The magnitude and shape if this pressure load depends on the type, shape and weight of the explosive, as well as the distance to the explosive charge. The interaction with surfaces will reflect and possibly amplify the pressure wave, depending on the angle between the surface normal and the direct line from the explosive charge to the target surface. This angle is called the angle-of-incidence, and is denoted by the symbol α. Furthermore the shortest distance from the charge to the surface target is known as the stand-off distance, R. These parameters are shown in figure 3.2. If the angle-of-incidence is 90° the blast wave travels parallel with the surface and we have what is called side-on loading. If the angle is 0°, the blast wave hits the surface perpendicularly and we have head-on loading. The two cases are shown in figure 3.3.

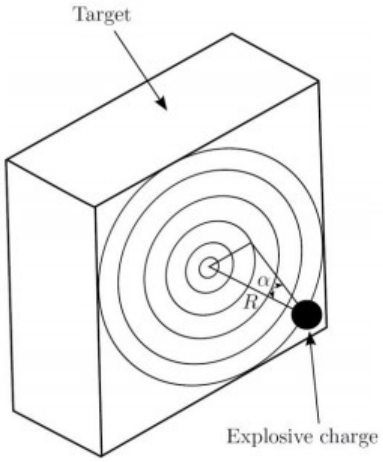

Figure 3.2: Angle-of-incidence and stand-off distance. *Adapted from Aune et al.[21]*

For all other cases than side-on loading the blast wave is reflected off the the surface, resulting in a reflected blast wave of the same form as the incident blast wave. For side-on loading the loading pressure is equal to the incident pressure. Otherwise the reflected pressure can be over 10 times as large as the peak incident pressure, depending on angle of incidence [21]. The pressure increase from reflection is caused by the air particles colliding with the surface are partly prohibited from bouncing back by the subsequent incoming particles. Because the air particles are unable to escape the shock wave is

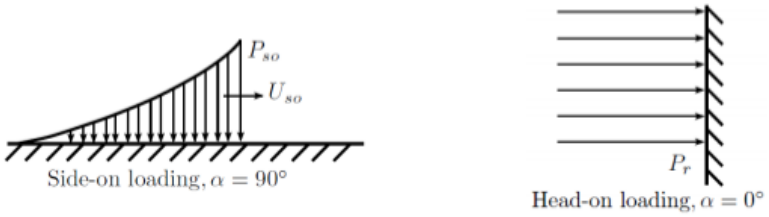

Figure 3.3: Side-on and head-on pressure loading.*Adapted from: Cormie et al.[24]*

compressed, increasing the pressure on the structure. Accounting for this increase is of paramount importance as the reflected pressure is the one that actually loads the structure. A typical equation used to represent the pressure loading from an ideal blast wave acting on a structure is the Friedlander equation, shown below.

$$P(t) = P_0 + P_r\left(1 - \frac{t}{t_+}\right)e^{\frac{-bt}{t_+}} \tag{3.2}$$

Here P_0 is the ambient pressure, P_r is the peak reflected overpressure, t_+ is the duration of the positive phase and b is a coefficient describing the pressure decay. Having a description of the time-pressure history, as described by the Friedlander equation and shown in figure 3.1, the impulse loading the structure, known as the specific impulse, can be found by integrating the area under the curve. Thus the specific impulse from e.g the positive pressure phase can be expressed:

$$i_s = \int_{t_a}^{t_a+t_+} P_r(t)dt \tag{3.3}$$

Using the reflected pressure from the Friedlander equation the specific impulse can be calculated:

$$i_s = \frac{P_r t_+}{b^2}\left(b - 1 + e^{-b}\right)$$

When a pressure wave is reflected at an angle, it is distinguished between ordinary reflection and Mach reflection. For an angle of incidence lower than approximately 40 °, we have ordinary reflection where the wave reflects of the structure at a reflected angle, α_r. This reflected angle generally differs from the incident angle α. For $\alpha > 40°$ the incident wave can catch up with the reflected wave to produce a third shock wave known as the Mach front. This front is generally assumed to be a plane wave travelling parallel with the surface. The intersection point between the three waves is called the triple point. The height above the ground of the triple point grows larger as the distance from the explosion increases. This means that for structures far away the mach front is higher than the structure, giving a uniform pressure over the entire structure height. For more close-in explosions , the triple point will be located below the top of the structure, producing a pressure distribution that has a uniform distribution below the triple point, and the incident pressure distribution above it.

Blast environments

Blast environments are often discerned into three different categories depending on distance from the explosion originto the ground (H) and to the considered structure (R). If $H > R$, the environment is of the free airburst type, where the explosion happens in free air and the blast wave reaches the structure before it reaches the ground. The second category is the airburst blast environment, where the explosion also happens in free air, but the blast wave reaches the surface and is reflected before it reaches the structure. This environment typically produces a Mach front that loads a portion of the structure height. The final category is the surface burst blast environment, where the explosive is detonated in contact with or very close to the ground. This entails the blast wave immediately reflecting off the ground and then expanding hemispherically until it impacts the structure. The different blast environments are shown graphically in figure 3.4.

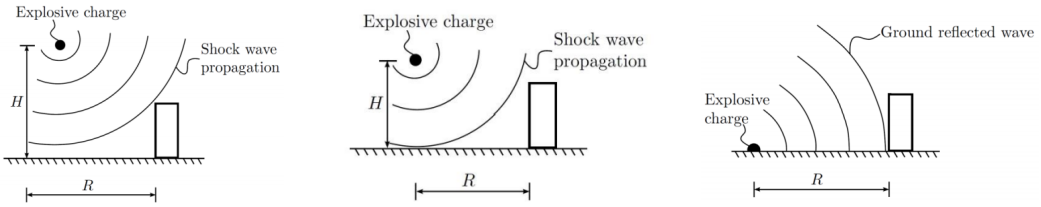

(a) Free airburst **(b)** Airburst **(c)** Surface burst

Figure 3.4: Blast environments. *Adapted from Aune et al. [21]*

Internal explosions

Internal explosions is a more complex blast environment where the blast wave is reflected off the surrounding surfaces and impacts with itself, repeatedly creating new shock waves until the pressure eventually is vented out and decays. The initial part of such explosions, dubbed the *shock pressure phase*, is similar as in unconfined conditions, where the sharp pressure peak impacts the environment. As the shock wave reflects of the confining surfaces the blast environment becomes much more complicated. High temperature gasses from the detonation expand in the confined volume, and will cause a pressure increase as they are not able to vent. This phase is often dubbed the *gas pressure phase*, and is of much longer duration than the preceding *shock pressure phase*. For confined explosions additional effects due to afterburn may also become significant, this will be further discussed in section 3.2.2.

Scaling Laws

As full scale testing is impossible in practice, scaling laws are needed to evaluate and compare tests at different scales. The most common scaling method is Hopkinson-Cranz scaling, also known as cube-root scaling. The method was independently developed by Hopkinson in 1915 [25] and later by Cranz in 1926 [26]. The method relates two blast scenarios of the same explosives and charge geometries, but with different charge weights and stand-off distances. The reference scenario has a stand-off distance R_{ref}, a total released energy from the explosion E_{ref}, and a charge weight W_{ref}. The relation

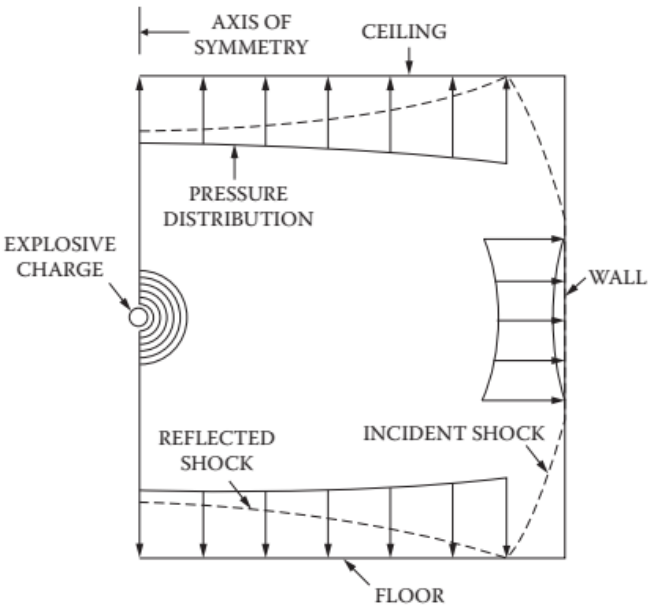

Figure 3.5: Visualisation of a confined explosion environment. *Adapted from Krauthammer [22]*

to a different scenario with stand-off distance R, total energy , and charge weight W is then given by equation 3.4. Here the charge geometry is assumed to be spherical, for which the blast parameters depend on the cube of the distance travelled (i.e. the stand-off distance).

$$\frac{R_{ref}}{R} = \left(\frac{E_{ref}}{E}\right)^{1/3} = \left(\frac{W_{ref}}{W}\right)^{1/3} \tag{3.4}$$

This relation is often simplified by setting E equal to a unit energy (e.g. 1 kJ) or W equal to a unit mass (e.g 1 kg), giving:

$$Z = R = \frac{R_{ref}}{W^{1/3}} = \lambda R_{ref} \tag{3.5}$$

or

$$Z = R = \frac{R_{ref}}{E^{1/3}} = \lambda R_{ref} \tag{3.6}$$

Where Z is the *scaled distance* and λ is a scaling factor depends on whether the scaling is done with regards to charge weight or energy released. The former is normally used when considering chemical explosions, giving a scaling factor of $\lambda = \frac{1}{W^{1/3}}$.

As mentioned the Hopkinson-Cranz scaling method assumes spherical explosive charges with cube-root scaling, but similar approaches can be done for other charge geometries. For instance a charge with a cylindrical geometry could be expected to have square-root scaling, where the arising blast wave expands circularly with the shape of a cylinder.

Loading categories

The scaled distance allows for a simple distinction between different loading categories. This is convenient as the blast wave distribution and pressure magnitude depend strongly on explosive charge size and stand-off distance, which are both included in the scaled distance Z. Based on Z the loading category is considered close-in, near-field or far-field.

$$\begin{aligned} \text{Close-in} &\quad Z \leq 0.5 \\ \text{Near-field} &\quad 0.5 \leq Z \leq 2.0 \\ \text{Far-Field} &\quad Z \geq 2.0 \end{aligned} \tag{3.7}$$

The loading category typically gives an indication of the response and damage one can expect to occur in a structure. When the scaled distance increases and the category is far-field the response is generally global, as the blast wave becomes uniform over the entire structure.

3.2.2 Afterburn

Afterburn is the process of products of the detonation mixing with the air and combusting. The process is visible as the arising fireball that is popularly considered a typical feature of an explosion. It produces significant heat development, but is much slower than the instant detonation process. Because of this, afterburn has a small effect on the structure response for free air explosions. This is due to the heat being able to dissipate and the temperature decreasing, which in turn allows the pressure to decay. Furthermore the afterburn mixing process itself requires high temperatures to maintain, and thus the process stops before all the available detonation products have time to oxidize. In confined spaces on the other hand, the heated air is unable to escape, the temperature is kept high, and the volume develops high pressures. Because of the longer duration of the afterburning, the pressures also decay slower than in open space, affecting the structure for a longer time, which in turn increases the total impulse.

Explosives that are able to produce afterburning are called thermobaric, in essence meaning that they are fuel-rich. During the detonation process

The general process of afterburning in free air has by several authors been divided into four separate stages [27] [28]:

1. Strong blast wave: The initial blast wave from the detonation pushes the mixing layer of detonation products and air outwards. A rarefaction wave propagates inwards and creates a secondary shock wave, and the mixing interface is accelerated. Instabilities due to a density gradient over the interface causes turbulent flow, increasing the mixing rate.
2. Implosion: The expanding detonation product gases strengthens the secondary shock wave, which eventually implodes, reducing the volume of the mixing region.
3. Reshock: Implosion at the origion reflects the secondary shock wave outwards again, where it interacts with the mixing layer yet again. Further instabilities arise, increasing the reaction rate and expanding the fireball.
4. Asymptotic mixing: The final phase where the pressure in the mixing layer stabilizes and the remainder of the detonation products is combusted.

3.2.3 Predicting Blast Loading

In order to design and assess the response of structures exposed to blast loading, methods for predicting the blast parameters (e.g. peak pressure, impulse, etc.) on the structure are needed. In general it's convenient to distinguish between three types of methods: empirical, semi-empirical and numerical.

Empirical Methods

Empirical methods provide relatively simple relations to predict loads based on sets of experimental data. They offer decent accuracy, but are only valid for the specific range of parameters in the experiments. Empirical methods are mostly utilised to model simple cases, and are generally valid only for long stand-off distances where the blast wave can be considered uniform over the structure. Thus these methods become increasingly inaccurate for more complex blast scenarios, such as confined or close-in explosions.

Eurocode EN 1991-1-7: Accidental loads on structures [29] offers an empirical approach for design of structures subjected to internal explosions. For explosions in road and rail tunnels the pressure history from either detonation or deflagration can be found from a set of simple equations (given in appendix A.1). Figure 3.6 gives a graphical representation of these pressure-time relations. While the Eurocode offers a simple approximating method, it only considers a specific case and should be supplemented with more advanced methods when studying more advanced scenarios.

Among the most common empirical methods are the empirical equations developed by Kingery and Bulmash [30]. The equations are high order polynomials curve-fitted to a large empirical database from experiments with TNT charge sizes in the range 1 to 400 000 kg. The empirical data is from idealised conditions at sea level. Furthermore, most of the experiments are for scaled distances larger than $0.4 m/kg^{1/3}$, and the equation thus have limited validity for close-in blasts. When the the Hopkinson-Cranz scaled

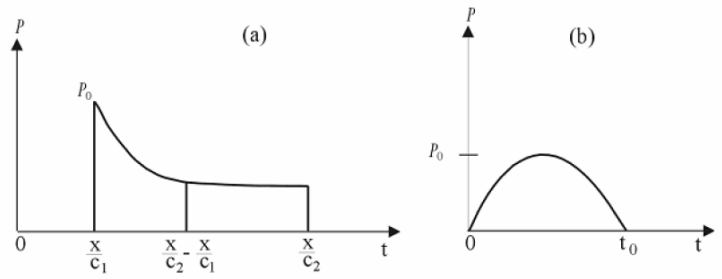

Figure 3.6: Pressure histories from detonation (a) and deflagration (b) for internal explosions in rail and road tunnels. *Adapted from NS-EN 1991-1-7 [29]*

distance is known, the equations utilizes the Friedlander equation 3.2 to produce blast parameters for the two cases of hemispherical surface burst and spherical free airburst. For visualization the equations are shown graphically shown in figure 3.7 for the case of a spherical free airburst. For the case of hemispherical surface bursts, the graphs would qualitatively be similar, but with larger values due to the immediate surface reflection. The plotted parameters are as follows: P_r is the peak reflected overpressure, P_{so} is the peak incident overpressure, i_r is the specific reflected impulse, i_{so} is the specific incident impulse , t_+ is the positive phase duration, t_a is the time of arrival, and u_s is the shock wave velocity

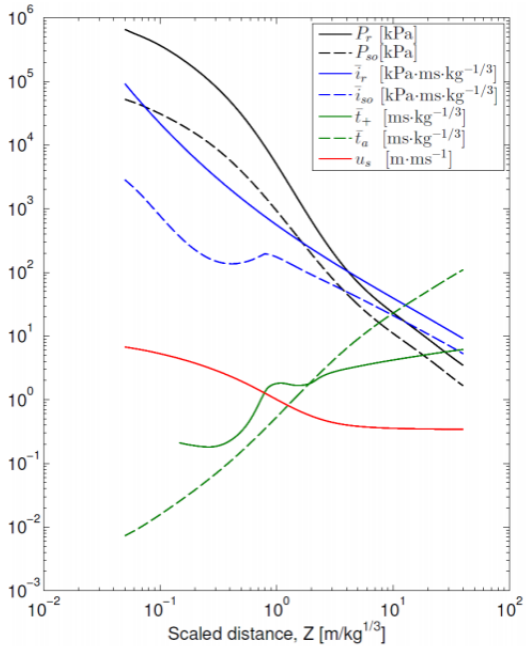

Figure 3.7: Kingery-Bulmash blast parameters for spherical free airburst. *Adapted from Aune et al.[21]*

The work of Kingery and Bulmash also form the foundation upon which many differ-

ent tools and manuals are built. Among these is ConWep (the Conventional Weapons Effects Program). ConWep is an example of such a tool that calculates blast loading based on the simple input of explosive type and weight, along with stand-off distance. It offers a simple way of approximating the loading and is included in included in many finite elements codes.

Semi-Empirical Methods

Semi-Empirical Methods are also based on experimental data, but additionally take into account certain geometry effects. Such effects can be partially or wholly confined surroundings. These methods still don't attempt to solve the relations and equations of the underlying physics, but offer a more accurate estimation of the the blast load, at the cost of increased complexity. As many of these methods are developed and used by military defence agencies, their availability is limited, and they will not be considered further in this thesis.

Numerical Methods

Numerical methods have a basis in Computational Fluid Dynamics (CFD), and offer the most complex and realistic method for reproducing the blast phenomenon. CFD models divide a considered domain into discrete volumes for which numerical calculations can be done according to the governing equations of fluid mechanics (conservation of mass, momentum and energy). These methods are capable of capturing the underlying physics of the blast phenomenon and are thus better suited for scenarios with varying geometries. The downsides of these methods are increased computational costs and comprehensive modelling needs.

The motion of matter is described either by a Eulerian or a Lagrangian formulation. An Eulerian mesh is fixed in space and allows for matter to flow between the finite volumes, and is therefore suitable for describing fluid motion. The Lagrangian formulation follows the matter, and will deform along with it, making it suitable for the structural subdomain. In hydrocodes the response of the structure is generally not considered, and the structural members are modelled as rigid boundary conditions that obstruct and reflect the fluid flow. A Eulerian formulation is used to describe the behaviour of the air and the detonating explosive, and the pressure history on the rigid boundaries(structure) is calculated. Subsequently this pressure history can be applied to e.g a finite element model of the structure, which uses the Lagrangian formulation. This is dubbed an uncoupled approach, as the structural deformation will not influence the behaviour of the fluid, or vice versa. This fluids-structure interaction is addressed further in section 3.2.5.

Applying CFDs to simulate blast loading requires the inclusion of an equation of state (EOS). An EOS is an equation that describes the state of a given matter by relating it's state variables such as pressure, volume, temperature. A common example of an EOS is the ideal gas law [31]:

$$pV = nRT$$

which relates the pressure p, volume V, temperature T and the number of moles in a gas n by use of the universal gas constant $R = 8.3145\ J/(K \cdot mol)$. The ideal gas law can be used for blast modelling if one only wishes to simulate the gas expansion phase. Should the detonation process and transition from solid explosive to gas be simulated as well, the ideal gas law comes up short because it is unable to represent phase transitions. In such cases the Jones-Wilkins-Lee (JWL) given equation of state, given below, is widely used.

$$p = A\left(1 - \frac{\omega}{R_1\bar{\rho}}\right)e^{-R_1\bar{\rho}} + B\left(1 - \frac{\omega}{R_2\bar{\rho}}\right)e^{(-R_2\bar{\rho}} + \omega\rho e_0 \tag{3.8}$$

A, B, R_1, R_2, and $\omega = \gamma - 1$ are parameters depending on the explosive material, e_0 is the internal chemical energy in the explosive, and $\bar{\rho} = \rho_{exp}/\rho$ is the relative density between the solid state density ρ_{exp}, and the detonation product density ρ. Here $\gamma = C_p/C_v$ is the ratio of specific heat at constant pressure to the specific heat at constant volume.

3.2.4 Structural Response to Blast loading

The next step is assessing the response and potential damage of the structure.

Pressure-Impulse diagrams

Pressure-Impulse diagrams is an efficient tool that provides a quick way of assessing structural response to blast loading in the early design phase. When a maximum level for damage or displacement is given, the P-I diagram displays the combination of pressure and impulse that causes damage exceeding the threshold value. In the example in figure 3.8 the region below and to the left of the curve indicates no damage, while the region above and to the right of the curve is where damage will occur.

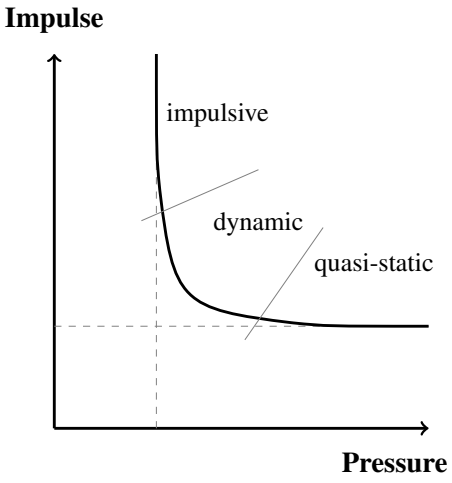

Figure 3.8: Example of a pressure-impulse diagram

The relationship between the duration of the loading, t_d, and the response time of a structure, here represented by the natural frequency ω_n, is an important indicator for the structural response, and is used to discern between three different loading regimes: the quasi-static, the dynamic, and the impulsive. In literature (e.g Baker et al. [32]), the following rule of thumb is often used as a set of quantifiable limits for the different regimes:

$$\begin{aligned} \text{Impulsive} \quad & \omega_n t_d < 0.4 \\ \text{Dynamic} \quad & 0.5 < \omega_n t_d < 40 \\ \text{Quasi-static} \quad & \omega_n t_d > 40 \end{aligned} \tag{3.9}$$

When the load duration is long compared to the structural response time we are in the quasi-static regime, and the load is still close to its peak at the time of maximum displacement. The response is only dependent on the structural stiffness and the peak load value, and the load history is of little importance. For the impulsive regime the load duration is much shorter than the structural response time, and the load is removed before the system has time to respond. The structural response is also is this regime independent of the load history. The dynamic regime is situated between the other two regimes, and the structural response time is of the same order of magnitude as the load duration. This regime is far more complex than the other two, and the structural response is highly dependent on the load history.

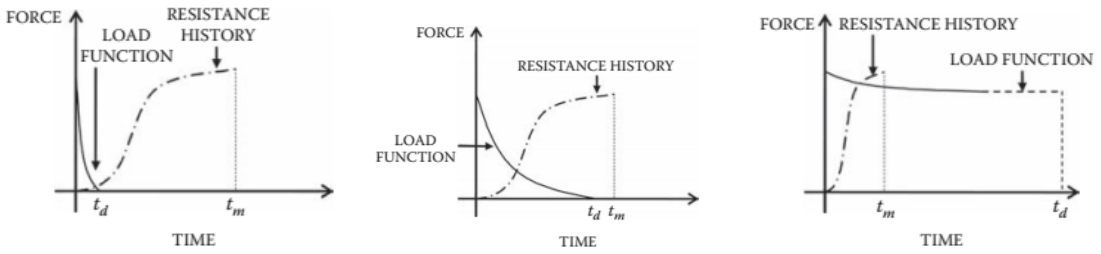

(a) Impulsive **(b)** Dynamic **(c)** Quasi-static

Figure 3.9: Load functions and response times in the different loading regimes. *Adapted from Krauthammer [22]*

3.2.5 FSI

Numerical methods are also capable of calculating structural response alongside the blast loading, incorporating the interaction between the two by using Fluid Structure Interaction (FSI) algorithms. While the structural subdomain is discretized by finite elements, the fluid subdomain can be discretized by either finite elements or finite volumes, although the latter is the normally preferred. FSI couples the two subdomains and allows them to interact. The simplest method is the uncoupled approach, as described in the numerical methods paragraph in section 3.2.3.

A more complex, coupled, approach is the Arbitrary Lagrangian Eulerian (ALE) method, where the Eulerian fluid mesh follows and is coupled to the Lagrangian structural mesh. The coupling is enforced through a strong or a weak approach. The strong approach enforces constraints on the nodal velocity at the interface boundary, but is incapable of

modelling larger structural deformation or failure. The weak approach enforces no constraints, and directly applies pressure loads from the fluid to the structural boundaries. With significant deformation re-meshing may be required, as the boundary between the two domains moves. This can cause high computational cost along with a loss of accuracy.

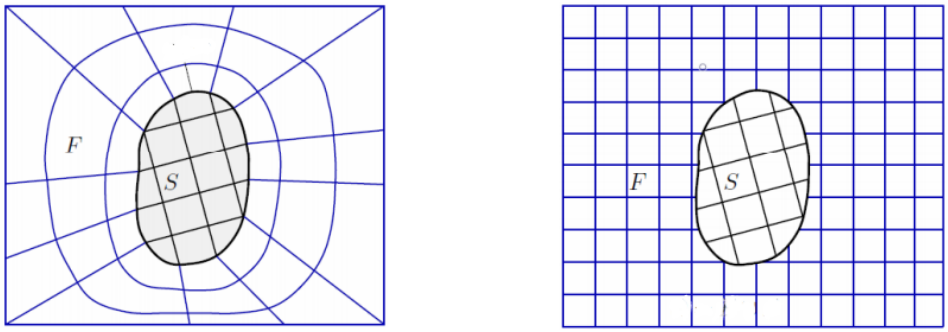

(a) ALE mesh **(b)** Embedded mesh

Figure 3.10: Meshing of Fluid (F) and Structural (S) domains for the coupled approaches. *Adapted from Aune et al. [21]*

A second, coupled, approach discretizes the fluid and structural subdomains independently. The structural mesh is embedded in the fixed fluid mesh, where it is allowed to move around without the need for altering the fluid domain. Thus such methods are dubbed embedded, overlapping, immersed, or ficticious domain mesh methods. The meshing for the two coupled approaches are illustrated in figure 3.10. Identifying which fluid nodes lies on the interface between the domains is the main challenge of the embedded mesh method. It is done by adding spheres of a chosen radius around each structural node, and connecting them through prisms or hexahedra. This creates an influence domain that contains all the coupled nodes, see figure 3.11. Chosing an appropriate radius is of high importance, as a too high value will couple an excessively large portion of the fluid domain to the structure, while a too small value will cause artificial fluid flow across the structure. When the influence domain has been identified, coupling on the interface can be enforced through either the weak or the strong approach, as for the ALE method. Further reading on embedded mesh methods can be found in the literature, e.g. [33].

3.3 Finite Element Analysis

Finite element methods (FEM) is a powerful numerical tool that enables assessing complex structural and mechanical problems that are beyond the capabilities of analytical methods. A continuous structure is discretized into finite elements connected by nodes at their boundaries. This reduces the problem into a set of equations where the unknowns are the nodal displacements. The element behaviour depends only on the nodal

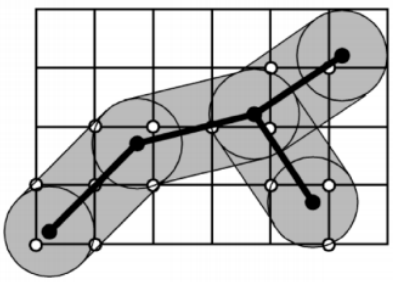

Figure 3.11: Influence domain. *Adapted from []*

displacements, and the full structural response can thus be obtained. This section is mainly based on the work of Hopperstad & Børvik[34]. Where other sources are used, this will be stated.

For most common problems the behaviour of the structure can be assumed linear, which simplifies the solution process. however, in the case of concrete pipes subjected to blast loading these assumptions are no longer valid due to nonlinearities. Among these are interaction between fluid (air) and structure, material nonlinearity (including possible fracture) and possibly geometric nonlinearities due to significant deformation. A non-linear FEA approach is thus necessary.

3.3.1 Explicit FEA

In the realm of dynamic nonlinear analyses a direct integration scheme is applied to solve the equation of motion in time. The equation of motion for a dynamic system is:

$$\boldsymbol{M}\ddot{\boldsymbol{u}} + \boldsymbol{C}\dot{\boldsymbol{u}} + \boldsymbol{K}\boldsymbol{u} = \boldsymbol{R}^{ext} \tag{3.10}$$

Here $\boldsymbol{u}$ is the vector of nodal displacements, and $\boldsymbol{M}$, $\boldsymbol{C}$, and $\boldsymbol{K}$ are the mass, damping, and stiffness matrices respectively. $\boldsymbol{R}^{ext}$ is the external force vector. A distinction is made between explicit and implicit based on the time integration scheme. For transient problems including wave propagation due to e.g. blast loads the explicit method is preferable due to the need for shorter time steps to capture the response accurately. The explicit method is based on the central difference time integration scheme, illustrated in figure 3.12. The unknowns at time t_{n+1} is calculated as in equations (3.11) – (3.13), where they can be found purely from known values at the previous timesteps. This is what makes the method explicit, and each time step is computationally inexpensive.

$$\dot{\boldsymbol{u}}_{n+1} = \dot{\boldsymbol{u}}_{n-\frac{1}{2}} + \frac{\Delta t_{n+1} + \Delta t_n}{2}\ddot{\boldsymbol{u}}_{\boldsymbol{n}} \tag{3.11}$$

$$\boldsymbol{u}_{n+1} = \boldsymbol{u}_{\boldsymbol{n}} + \Delta t_{n+1}\dot{\boldsymbol{u}}_{n+\frac{1}{2}} \tag{3.12}$$

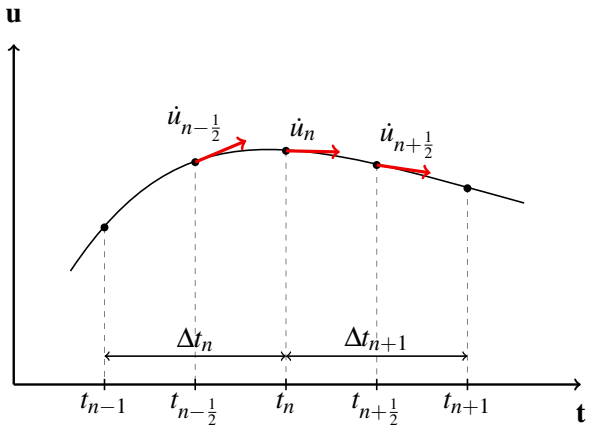

Figure 3.12: Central difference time integration scheme with time increments and velocity vectors

$$\ddot{\boldsymbol{u}}_{\boldsymbol{n}} = \boldsymbol{M}^{-1}\left(\boldsymbol{R}_{\boldsymbol{n}}^{ext} - \boldsymbol{R}_{\boldsymbol{n}}^{int}(\boldsymbol{u}_{\boldsymbol{n}})\right) \tag{3.13}$$

Stability

The explicit time integration is only conditionally stable, and requires a sufficiently small time step to convergence to an accurate solution. The critical time step depends on the mesh size and the material properties, and is given as:

$$\Delta t_{cr} = \frac{L^e}{c_d} \tag{3.14}$$

where L^e is the characteristic length of the smallest element in the model, and the dilatational wave speed c_d is given by:

$$c_d = \sqrt{\frac{E}{\rho}} \tag{3.15}$$

where E and ρ are the Youngs modulus and density of the material. The critical time step is thus the time it takes a stress wave to propagate the length of the smallest elements, and the applied time step must be shorter than this to ensure information is not lost.

Mass and time scaling

The necessity of short time steps makes the explicit method suitable only for problems of short duration. Workarounds does however exist to make it feasible also for quasi-static problems, namely mass and time scaling. From equations (3.14) – (3.15) it can be seen that artificially increasing the density by a factor k allows for an increase of the critical time step by a factor $\sqrt{k}$. Another method is scaling down the actual time of the problem in the finite element model to a duration which is viable for the explicit method. Both

mass and time scaling must however be used with care for quasi-static problems. As to ensure that dynamic effects are negligible, energy balance checks should be conducted to make sure the kinetic energy is small compared to the kinetic energy.

Hourglassing
In explicit FEA reduced integration of elements is often used to reduce computational costs. Reduced integration reduces the number of integration points over an elements in calculating the stiffness matrix, but will introduce spurious zero-energy modes. As a remedy for this hourglass control is applied, in which artificial stiffness is added to the model to avoid the zero energy modes of hourglassing. Introducing artificial stiffness may naturally affect the model behaviour, and an energy check should be conducted to ensure the artificial energy is negligible compared to the internal energy of the model.

THIS PAGE INTENTIONALLY LEFT BLANK

Chapter 4

Concrete

Concrete is a widely used material on account of its availability, low cost, and versatility. It is furthermore the preferable material for the construction of an SFT.

4.1 Composition

Concrete is a heterogeneous, composite material consisting of aggregates of varying sizes distributed in a cement matrix or paste. Fresh concrete is a mix of water, coarse and fine aggregate, cement, and possibly additional pozzolans such as fly ash and silica fume. Additionally admixtures may be added to obtain or improve certain properties, e.g. frost resistance, and workability. In describing a concrete mix one of the most important parameters is the water-/cement ratio w/c. Generally, a lower w/c-ratio means a higher strength concrete as the excess water in time evaporates, increasing porosity in the fresh phase[35]. Lowering the w/c-ratio also has negative effects, primarily affecting the workability in the fresh phase, making it harder to adequately compact the concrete in the desired shape.

Concrete is classified based on its compressive strength, and is denoted as e.g C20/25, where the numbers indicate minimum cylindrical and cubical compressive strengths of 20 and 25 MPa respectively. Concrete in the range C20/25–C40/50 is used in most applications, but high strength concrete up to C100/115 is available for structures with special strength requirements. The concrete strength classes are based on the mean strength measured 28 days after casting, f_{cm}. Strength of the concrete after $t < 28$ days of hardening can be estimated from:

$$f_{cm}(t) = exp\left\{ s\left[1 - \left(\frac{28}{t} \right)^{1/2} \right] \right\} f_{cm} \tag{4.1}$$

where s is a coefficient dependent on the cement type. Under the right conditions the concrete will continue to harden well past 28 days, increasing the strength further.

The strength of concrete is notably lower than the individual strength of its two components: aggregate and cement paste. The explanation lies in a third part, namely the interfacial transition zone (ITZ), that lies between the aggregate and the paste in hardened concrete. The ITZ is formed during the curing process when the cement particles are unable to evenly distribute around the larger aggragate particles because of the wall effect [36], leading to a higher local porosity and w/c-ratio in this area. In turn this causes weaker hydration products and a higher porosity in the ITZ. Thus the strength of the transition zone is lower than in the rest of the matrix. Additionally, small cracks known as shear-bond cracks are formed in proximity of the larger aggregates during the hardening phase. Due to the influence of the interfacial transition zone, concrete is often considered a three-, rather than a two-phase material.

4.2 Mechanical properties

The heterogeneous and complex The shear-bond cracks arises prior to any loading of the specimen. When a load is applied, these cracks expand and connect with new cracks arising in the cement matrix. They eventually form a continuous cracking system and the material fails. Cracks in the interfacial transition zone require less energy to propagate than in the rest of the matrix, and will start expanding at stresses of about 30% of the ultimate strength. An increase in stress from this point leads to a disproportionately high strain increment, meaning that the originally linear stress-strain relationship starts to curve. When the stress reaches 75% of the ultimate stress, the mentioned crack propagation in both the ITZ and the matrix takes place, leading to further arching of the $\sigma - \varepsilon$-curve. This is the reason why concrete displays an inelastic behaviour as the stress increases. [35].

The stress-strain curve of concrete is qualitatively similar in uniaxial tension and compression, but significant quantitative differences are present. A rule of thumb is that the tensile strength is only about 10% of the compressive strength [35]. As a consequence, concrete is often assumed to have no tensile strength in the design phase, and steel reinforcement bars are added to carry the tensile forces. Under compression loading, crack propagation is restricted at lower stresses, and their growth beyond a certain limit is quickly arrested. Further propagation of the cracks in the ITZ requires introducing more energy through a higher load in accordance with the previous paragraph. This accounts for concrete displaying some ductility in compression, in contrast to the brittle failure one observes in both its constituents: cement matrix and aggregate. The crack propagation under tensile loading is much more rapid, as the cracks are arrested to a much smaller degree. Because the cracks propagate in a direction normal to the stress under tension, the crack formation will reduce the load-bearing area, causing further stress increase, which again drives the crack propagation. This causes concrete to fail in a brittle manner under tensile loading, and at much lower stress values than in compression.

Confinement and bi- or triaxial stress states has significant influence on the mechan-

ical response. Biaxial compression is seen to further impede crack propagation, and leads a potential strength increase of almost 30 % [35]. As tensile loading does not confine crack growth, no such effects are observed in biaxial tension. The different strength observed in cubical and cylindrical specimens are explained by confinement effects. For standard specimen geometries, the ratio between the contact surface and specimen height are larger for cubes than for cylinders. The confinement pressure from the frictional forces are thus for the cubes, allowing it to resist higher stresses.

As concrete has a slightly nonlinear inelastic behaviour, the elastic stiffness modulus can be approximated as one of three different elastic moduli: the tangent, secant, and chord moduli. The secant modulus is found as the slope of a line between the origin and the point on the $\sigma - \varepsilon$-curve at 40 % of the ultimate strength, as shown in figure 4.1 In Eurocode 2, the secant elastic modulus can be approximated to vary with time when the compressive strength is know [37]:

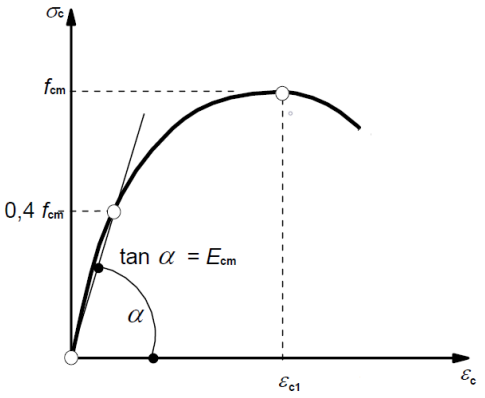

Figure 4.1: Secant modulus of elasticity from a typical stress-strain relationship for concrete. *Adapted from Eurocode 2. [37]*

$$E(t) = (f_{cm}(t)/f_{cm})^{1/3} E \tag{4.2}$$

In literature it is generally agreed upon that concrete exhibits a strength, as well as a stiffness increase as the load-rate increases[35] [38].

4.3 Failure modes

Concrete subjected to blast loading may experience damage of several different kinds leading up to failure. Among these are spalling/scabbing, cracking, cratering. At lower damage levels the concrete typically exhibits smaller amount of surface cracking along with spalling of thin pieces on the side facing away from the blast origin. On the blast side a crater may form due to material being pushed away laterally by the blast wave. Cracking generally occurs due to tensile stresses growing higher than the tensile strenght of the concrete [35]. For lower blast loads the cracks may only be superficial, but they may propagate through the thickness if exposed to high enough loads. As cracking increases pieces of the concrete eventually falls off or is blasted away, which is known as fragmentation.

4.4 Numerical modelling

On account of its inhomogeneity, rate dependency and complex microstructure concrete is material that is hard to model correctly. This is particularly true for complex loading

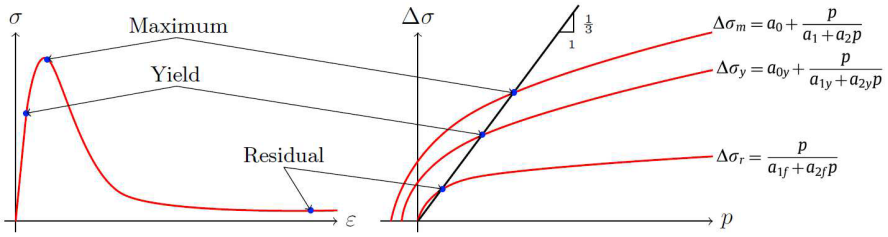

Figure 4.2: Failure surfaces of the K&C model. *Credit: Krone [18]and Hillestad and Pettersen [17]*

scenarios such as blast loading. In this thesis the Karagozian & Case concrete model (K&C) will be applied in LS-DYNA to model the material behaviour.

Karagozian & Case Concrete model The Karagozian & Case concrete model (K&C) is a material model designed to describe the behaviour of concrete when subjected to dynamic loading. The model was first released in 1994, and has since seen two new iterations. The third – and current – release is available in LS-DYNA with the keyword *MAT_CONCRETE_DAMAGE_REL3 [39].

The K&C concrete model is a three-invariant model, using three failure surfaces (maximum, residual and yield) depicted in figure4.2.

The failure surfaces describes the deviatoric part of the strains, which is not coupled to the volumetric strains. The volumetric strains are on the other hand described by an equation of state. Strain-rate effects and damage are both included in the model, making it suitable for highly transient problems.

The model has a total of 49 parameters, but through parameter generation the only necessary input is the concrete compression strength. Further parameters may however be added for further fine-tuning.

Further information on the model is available in the article of Malwar et. al [9] [39], the creators of the model.

Chapter 5

Experimental material studies

5.1 Reinforcement steel tests

This section will present the experimental work on the reinforcement steel in the concrete pipes. This work was carried out at NTNU prior to the initiation of this thesis. The concrete pipes had both longitudinal (8mm diameter) and circumferential (6mm diameter) reinforcement bars. Dynamic and quasi-static material tests were carried out on specimens machined from both reinforcement directions. Furthermore, test specimens were gathered from both virgin material as well as from post-tested pipe areas of high deformation (middle of the pipe). The specimens were axisymmetric bars with geometry as shown in figure 5.1.

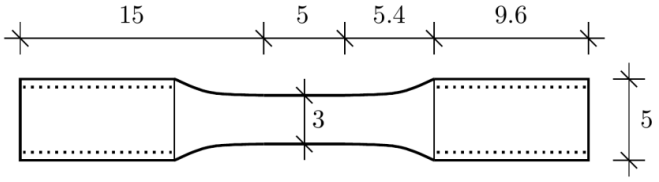

Figure 5.1: Geometry of reinforcement steel specimen

5.1.1 Material modelling

The reinforcement steel will modelled using the Johnson-Cook plasticity model [40]. Johnson-Cook plasticity is expressed by the following equation:

$$\sigma_{VM} = (A + Bp^n)(1 + C \ln \dot{p}^*)(1 - T^{*m}) \tag{5.1}$$

Here A, B, n, C and m are model parameters, p is the plastic strain and $\sigma_{eq} = \sqrt{\frac{3}{2}\sigma'_{ij}\sigma'_{ij}}$ is the von Mises equivalent stress, where σ'_{ij} is the deviatoric stress tensor. Furthermore,

$\dot{p}^* = \dot{p}/\dot{p}_0$ is the the dimensionless plastic strain rate, and $T^{*m} = (T - T_0)/(Tm - T_0)$ is the homologous temperature. In these equations, $\dot{p}$ is the plastic strain rate, $\dot{p}_0$ is a reference strain rate chosen by the user, T is the absolute temperature, T_m is the melting temperature of the material, and T_0 is the reference temperature (the ambient room temperature).

Failure is included in the model in form of the Cockroft-Latham fracture criterion [41]. The criterion is given in equation 5.2 below.

$$D = \frac{1}{W_C} \int_0^{p_f} \langle \sigma_I \rangle \, dp = \frac{1}{W_C} \int_0^{p_f} \langle \sigma^* + \tfrac{2}{3} \cos \Theta_L \rangle \sigma_{VM} \, dp \tag{5.2}$$

Here W_c is the fracture parameter, $\langle \sigma_I \rangle$ is the maximum principal stress, Θ_L is the lode angle, σ_{VM} is the von Mises equivalent stress. The angular set of brackets $\langle\rangle$, known as the Macaulay bracket, around the principal stress means the value is equal to zero if the maximum principal stress is negative, i.e. compressive. This means damage and fracture only occurs if the material experiences tension.

5.1.2 Uniaxial tensile tests

Quasi-static material tests were conducted in a general purpose Zwick testing machine with displacement control. A deformation rate of 0.15 mm/min was used, corresponding to an initial strain rate of $\dot{\varepsilon}_0 = 10^{-3}$ s^{-1}. During testing continuous measurements were made on force, crosshead displacement, and diameter reduction in two perpendicular directions. The latter was done through the used of a laser-based measurement device that allowed for monitoring the diameter of the specimens all the way to fracture. A total of 12 quasi-static tests were conducted. For each of the reinforcement directions, six tests were carried out: three on the virgin material and three on the post-tested material. Additionally dynamic material tests were conduced in a Split Hopkinson Tension Bar. The results were unfortunately omitted from this thesis due to time limitations.

5.1.3 Results

Measurements were smoothed using a moving-average filter in MATLAB.

The true stress from the quasi-static tests is plotted against the true strain for both reinforcement types in figure 5.2. The results show a difference in behaviour of the materials for the different reinforcement directions. The circumferential reinforcement exhibits higher yield and maximum stresses than the longitudinal reinforcement. The material seems to yields at roughly 600MPa.

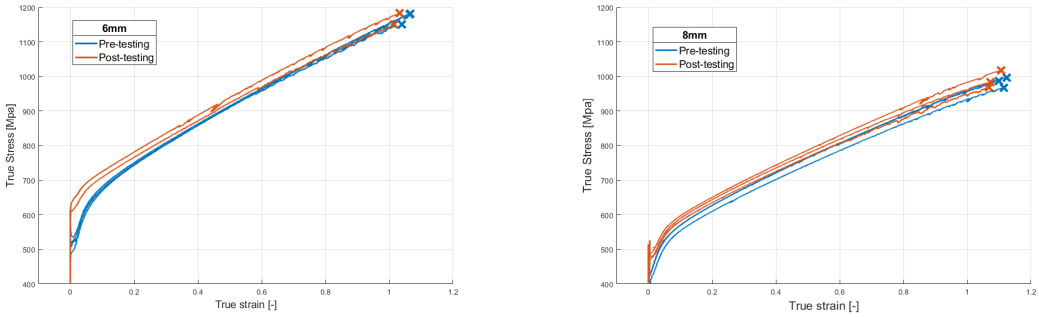

(a) Circumferential direction (6mm) **(b)** Longitudinal direction (8mm)

Figure 5.2: True stress-strain relations for reinforcement steel

5.1.4 Material model calibration

The Johnson Cook (JC) constitutive relation described in section 5.1.1 is here calibrated based on the experimental data. The relation is repeated here for reference:

$$\sigma_{VM} = (A + Bp^n)(1 + C \ln \dot{p}^*)(1 - T^{*m}) \qquad (5.1 \text{ revisited})$$

In the quasi-static tests strain-rate and temperature effects are assumed to be negligible, thus $T^{*m} = 0$, and that $\dot{p}^* = 1$. When necking occurs in the specimen, a complex, triaxial stress state arises, and the stress values need to be adjusted by the use of the Bridgeman-LeRoy correction:

$$\sigma_{eq} = \frac{\sigma_t}{(1 + 2R/a) ln(1 + a/(2R)} \qquad (5.3)$$

where the equivalent stress after necking σ_{eq} is calulated.σ_t is the true stress, R is the neck curvature radius, and a is the actual cross-sectional radius of the specimen. The ratio a/r is given as:

$$a/R = 1.1(\varepsilon_l^p - \varepsilon_{lu}^p)$$

Calibration of the steel material models unfortunately had to be omitted due to time limitations.

5.2 Concrete material testing

Uniaxial compression tests were conducted on concrete cubes and cylinders cut from the concrete pipes. The motivation was to determine the material properties of the concrete, as well as forming a basis of validation for the numerical methods. The test regimen

Table 5.1: Properties of the pipe concrete

w/c ratio	aggregate size	$f_c, cube$ (1 day)	$f_c, cube$ (7 days)	$f_c, cube$ (28 days)
0.37	0-8 mm	38.2 MPa	64.1 MPa	83.3 MPa

consisted of five cube compression tests, ten cylinder compression tests on two different cylinder sizes, and five splitting tensile tests.

Properties of the concrete produced by the supplier are summed up in table 5.1. The concrete density was further approximated at 2600 kg/m^3. With a 28-day cube compression strength of 83.3 MPa the concrete could be classified as B65.

5.2.1 Setup

The tests were performed in an Instron 5985 testing machine with a 250 kN load capacity. The deformation rate varied for the different specimen geometries, and corresponded to a strain rate of 1^{-4}. The force was continuously measured from the machine. A Basler acA2440-75um camera took continuous pictures at a frequency of 4 Hz for later use in the DIC software eCorr, which was used to obtain the specimen deformation. This made it possible to obtain the full stress-strain history until fracture. Prior to the testing the actual geometries of all specimens were measured.

5.2.2 Compression tests

Cube compression tests

The five cubes were cut out from the smaller pipes and machined into specimens of 40 mm nominal side length. Actual measurements showed some deviation from the nominal geometry, and are given in table 5.2. Some damage was observed along the cube edges and corners prior to testing. The deformation rate was set at 0.24 mm/min. The testing rig is depicted in 5.3

Figure 5.3: Setup of cube compression test

Cylinder compression tests

Cylindrical specimens with two different geometries were tested in compression. The larger cylinders had nominal height and diameter of 60 $\times$ 90 mm ($\phi \times h$), and were cut out from the large pipes. The smaller cylinders had nominal geometry of 30 $\times$ 40 mm ($\phi \times h$) , and

Table 5.2: Concrete cube measurements for compression tests

Cube #	Length (mm)	Width (mm)	Height (mm)	Weight (g)
1	40.28	40.2	40.11	158.1
2	40.28	40.40	39.20	156.3
3	40.15	40.19	39.05	153.7
4	39.70	39.38	39.83	151.9
5	39.94	40.26	38.24	150.2

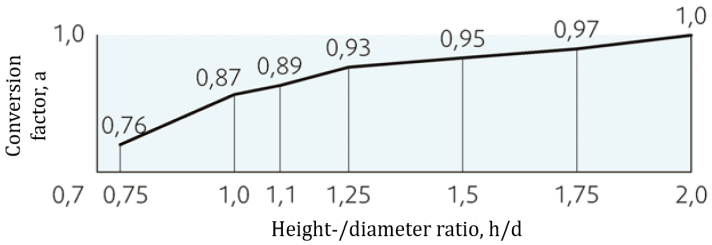

Figure 5.4: Correction factor for cylinder compressive strength of specimens with varying height-/diameter ratio. *Adapted from SINTEF Byggforsk 520.033 [43]*

were cut out from the small pipes. The measurements show some deviation from the nominal dimensions. All measurements can be found in the appendix B.1. For the large and small cylinders deformation rates of 0.564 mm/min and 0.24 mm/min were used, respectively. The ratio of cylinder height to diameter is representative of the slenderness of a specimen, and the standard NS-EN: 12390-1 for testing of hardened concrete [42] states that this ratio should be equal to 2 for standardised tests. For values lower than 2 the stress state cannot be considered one-directional any more. The height-/diameter ratio is 1.57 and 1.26 for the large and small cylinders respectively, and the compressive cylinder strengths are adjusted with a correction factor to obtain values equivalent to a cylinder with height-/diameter ratio of 2 (i.e uniaxial compressive strengths). Correction is done by the formula:

$$f_{c,cyl,corr} = a * f_{c,cyl}$$

wher the factor a can be found e.g from figure 5.4.

Tensile splitting tests

Additionally a third set of cylindrical specimens were cut out from the larger pipes. These specimens were more slender, with approximate diameter and height of 37 mm and 90 mm. Due to the slenderness machining the specimens to the nominal geometry proved difficult, and thus visible imperfections, in particular obliquity, were observed. Due to this it was decided to perform tensile splitting tests on these specimens, as the imperfections would be of less importance. Specimen measurements are included in appendix B.2.Two wooden strips are placed between longitudinal side of the specimen and the loading plates, as shown in figure 5.5. A deformation rate of 0.192 mm/min was used.

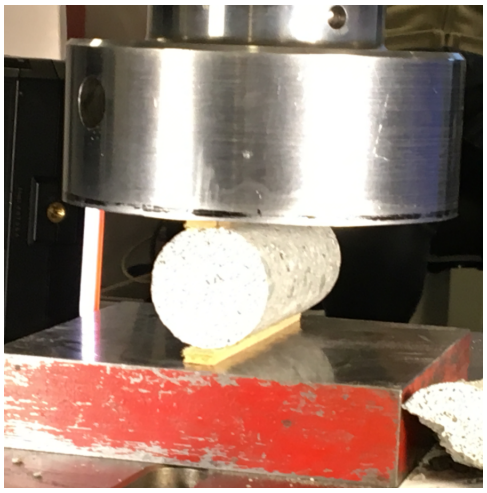

Figure 5.5: Setup of tensile splitting test

5.2.3 Dynamic concrete tests

Dynamic material tests on concrete specimen were conducted by Sunita Mishra et al. in a Split Hopkinson Pressure Bar(SHPB) at the Indian Institute of Technology (IIT) in Delhi. The results are presented here as a part of the studies on the concrete material behaviour. The main purpose of this studies is to find the dynamic increase factor (DIF) of concrete by comparing compressive strengths from dynamic and static tests:

$$DIF = \frac{f_{c,dynamic}}{f_{c,static}} \tag{5.4}$$

The results from the the SPHB tests had to be omitted due to time limitations, and are suggested for further work on the subject.

5.2.4 DIC

Digital Image correlation (DIC) is an optics-based measurement method that tracks deformation based on Typically DIC is applied for tests with ductile metals such as steel, for which the more continuous deformation is easier to track. Using DIC for concrete is more challenging as fracture happens instantly, and deformations are much smaller prior to fracture. However, encouraged by the promising results from the theses of Krone [18] and Skaare [19], the method should still produce decent measurements for concrete in the pre-cracking regime. The motivation for this section thus was to further assess this feasibility. All specimens were painted with a speckle paint prior to testing

to ensure a high-contrast surface pattern. This is essential for the optical analysis of the DIC software, and enables it to provide high quality displacement measurements.

DIC can be applied both for 2D and 3D measurements, however the latter requires a setup of two cameras and an extensive calibration. Only one camera and subsequently, 2D DIC, was used for the tests in this thesis. For the cube compression and splitting tensile tests this is perfectly adequate due to the plane surfaces measured. The curved surface of the compression cylinder specimens would require 3D DIC to measure the full displacement fields, and DIC was thus only used to track the longitudinal strain along the centre of the cylinder, as shown in figure 5.6b.

A more comprehensive analysis was conducted on the cubical specimens to study the capabilities of DIC with concrete as the material. The choice was made to focus on cube 1, and a structured Q4 rectangle mesh was used. Introductory analyses showed some numerical noise for a mesh size of 25x25 pixels, and the reference model was thus established with a mesh size of 50x50 pixels. A parameter study is conducted in following sections to assess the effect of the mesh size. Strain measurements were gathered from five virtual extensometers implemented as vectors over the loading direction, as depicted in figure 5.6a. The mesh was put well inside the cube edge to avoid any problems due to spalling. The bottom of the cube was also left out as the pre-damaged corner might affect the analysis.

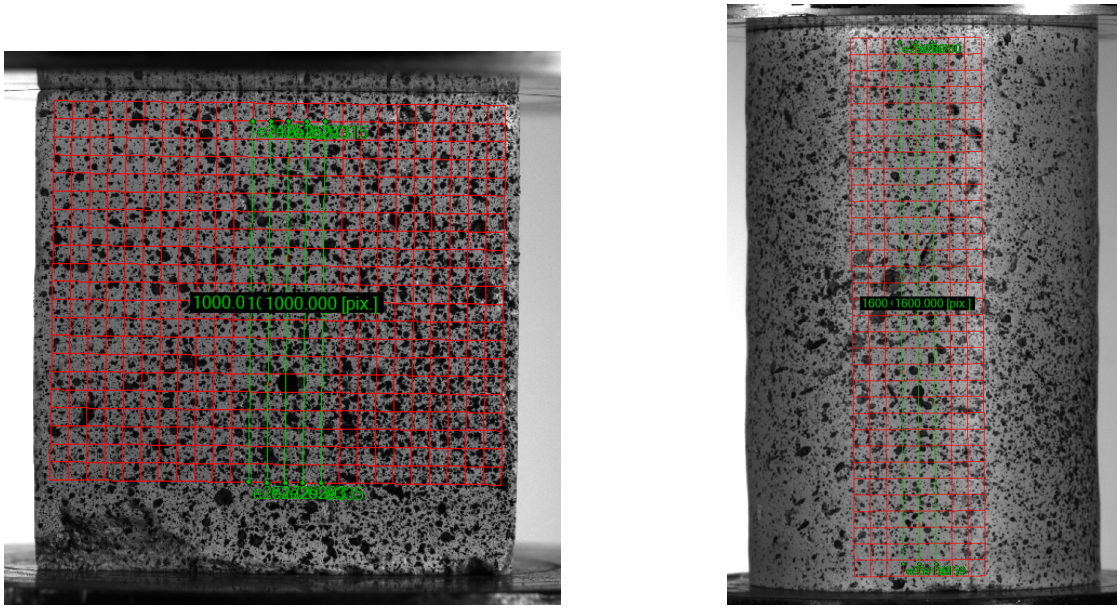

(a) **(b)**

Figure 5.6: DIC mesh for cubical (a) and cylindrical (b) specimens, with vectors (marked in green) for extraction of strain measurements

Figure 5.7 shows the first principal strain in the specimen just prior to failure. Some crack initiation is visible in in the specimen prior to this, but they are clearly accentuated

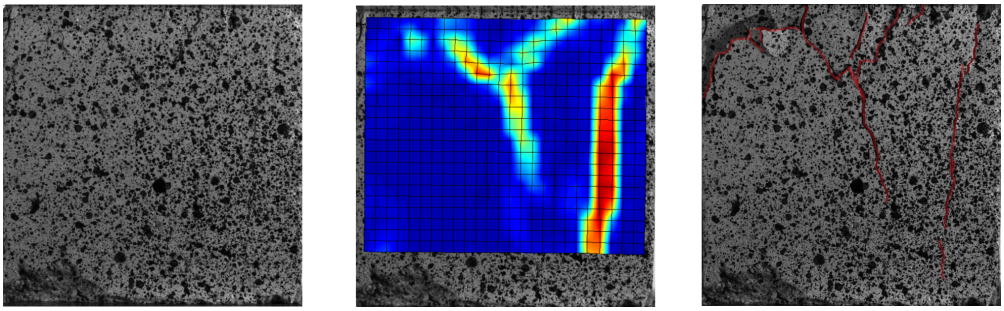

Figure 5.7: DIC crack prediction by using principal strains. The first and second picture are the specimen and principal strain at frame 1125; the third picture shows cracking, accentuated in red, in the specimen in the subsequent frame.

by the strain field in DIC. It also predicts the crack pattern in earlier frames, before it is visible to the eye.

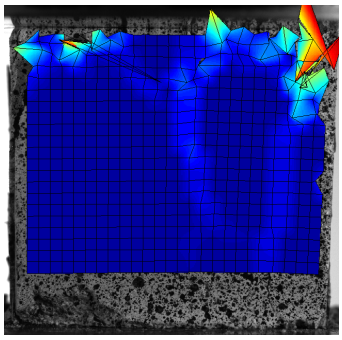

Figure 5.8: Mesh distortion in DIC analysis post-cracking

Engineering strains from the five vectors can be seen in figure 5.9. The strain measurements seem to linearly increase until around frame 900, where it takes a small dip before staying constant. The strains vector correspond well with each other until frame 1125, where the specimen fractures and the measured strains suddenly increase with rapid cracking. After this point the mesh becomes distorted, as seen in figure 5.8, and the strain measurements triple as the mesh loses correlation. The different vectors also separate from each other, due to non-uniform cracking across the cube.

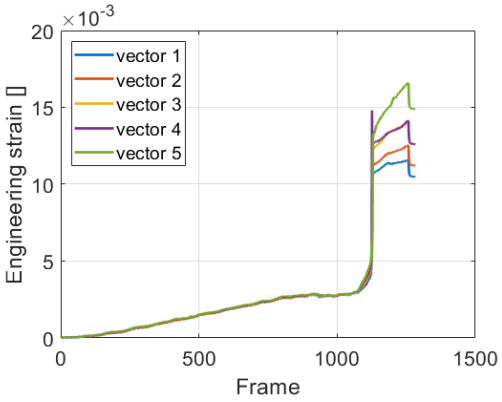

Figure 5.9: Engineering strain from

Mesh size effects

(a) Cubes

(b) Large Cylinders

(c) Small cylinders

Figure 5.10: Post-tested specimens from compression tests

In contrast to other discretization-based methods, like FEM, the accuracy of DIC decreases with mesh refinement. Smaller elements has a smaller basis for grayvalue comparision between frames, and is thus more likely to lead to loss of correlation and numerical noise in the strain measurements. Analyses with smaller elements of 25x25 pixels generally performed poorer in producing strain measurements, and an element size of 50x50 pixels were used in the remainder of the analyses. Smaller elements are however better at capturing the smaller cracks as they arise and give a more detailed visualisation of the strain field.

5.2.5 Results

Cube compression tests

Compression tests were conducted until after fracture of the specimen and some portion into the softening region. All fractured specimens are depicted in figure 5.10. Significant spalling and cracking damage is as expected observed on all specimens, leaving hourglass-shaped cores as particularly exhibited by cylinder 10.

The compressive strength is calculated as the peak force divided by the cross-sectional area of the loaded side of the specimens. Results from the compression tests on concrete cubes are shown in table 5.3.

Table 5.3: Results from compression tests on concrete cubes

Cube #	Peak force (kN)	Area (mm^2)	$f_{c,cube}$ (MPa)
1	132.57	1634.16	81.12
2	140.53	1639.84	85.89
3	138.45	1628.52	85.01
4	137.73	1580.19	87.16
5	143.86	1590.79	90.43

The average cubical compressive strength from the tests was 85.92 MPa, with a standard deviation of 3.02 MPa. The results are in good accordance with the stated strength from the supplier of 83.3 MPa. The small increase could be explained by the concrete tested here having more time to harden beyond the strength at 28 days.

Resulting engingeering stress-strain plots are shown in figure¨5.11 with deformation measurements logged from both DIC and the testing rig. For the testing rig strains are calculated as displacement divided by the specimen height (40 mm). For DIC the curves are plotted until convergence is lost in the analyses. Furthermore cube 4 was omitted from the DIC plots due to nonphysical strain fluctuations even long before the peak force was reached. The strain measurements from the testing machine is around an order of magnitude larger compared to the DIC, and are naturally much less stable as they are not affected by sudden cracking of the specimens. DIC should in theory be more in accordance with the actual strains, as it tracks the actual material deformations in contranst to just logging the loading plate displacement.

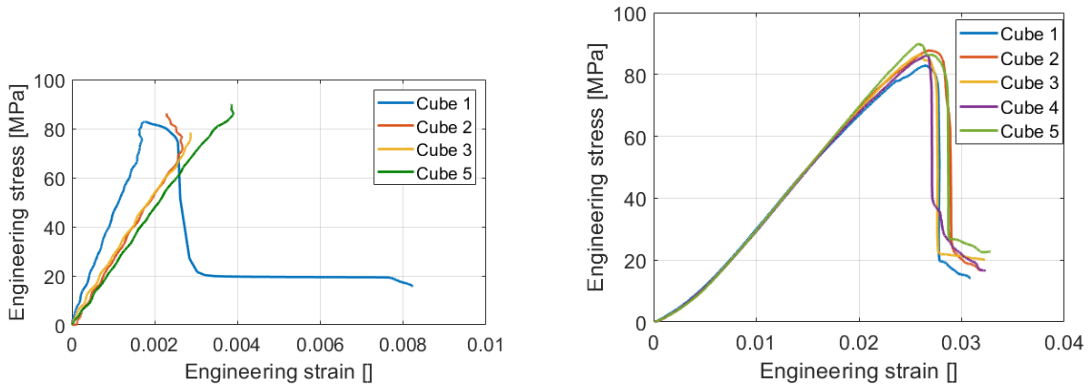

(a) DIC **(b)** Testing rig

Figure 5.11: Engineering stress-strain plots of cube compression tests from DIC measurements (a) and measurements from the loading rig (b).

Table 5.4: Results from compression tests on concrete cylinders

Cylinder #	Peak force (kN)	Area (mm^2)	$f_{c,cyl}$ (MPa)	$f_{c,cyl,corr}$ (MPa)
1	97.60	2750.68	35.48	33.92
2	101.05	2753.93	36.69	35.08
3	98.18	2755.79	35.63	34.06
4	106.02	2750.68	38.54	36.84
5	87.49	2753.00	31.78	30.38
6	70.94	838.79	84.58	78.74
7	66.44	844.71	78.66	73.23
8	73.24	843.68	86.80	80.81
9	68.57	843.42	81.29	75.69
10	66.28	843.16	78.61	73.19

For the larger cylinders the average compressive strength is 35.62 MPa and the standard deviation is 2.21 MPa. For the smaller cylinders the average compressive strength is 81.99 MPa and the standard deviation is 3.25 MPa. From figure 5.4 the correcting factors for height-/diameter ratio are 0.956 and 0.931 for the large and the small cylinders respectively. This gives corrected average compressive strength values of 34.06 MPa for the large cylinders and 76.33 for the small cylinders. This would classify the concrete as B75, or B65 if also accounting for the cubical strength, according to Eurocode 2 [37].

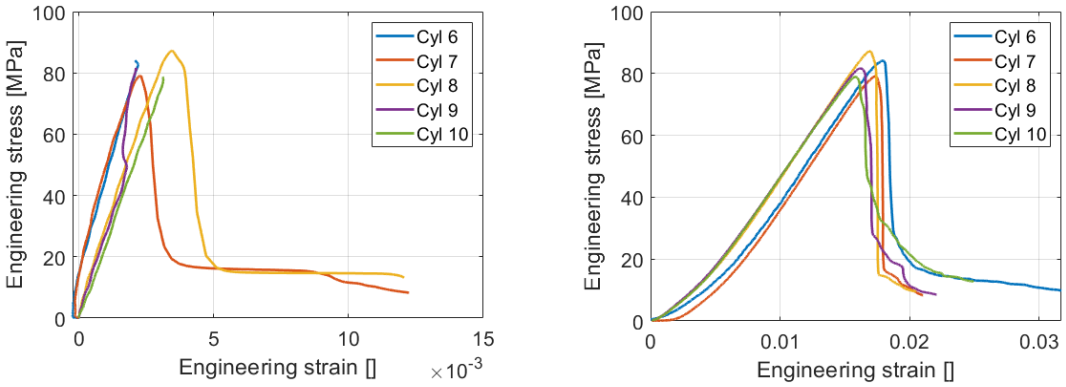

(a) DIC **(b)** Testing rig

Figure 5.12: Engineering stress-strain plots of small cylinder compression tests from DIC measurements (a) and measurements from the loading rig (b).

A large difference between the two specimen geometries is observed, with the smaller specimens exhibiting a compressive strength more than twice as high as the larger specimens. The different specimen geometries were cut from two different pipe sizes, but both were from the supplier stated to be of the same concrete type. The large discrepancy was therefore surprising. A possible explanation is the size effect as studied by del

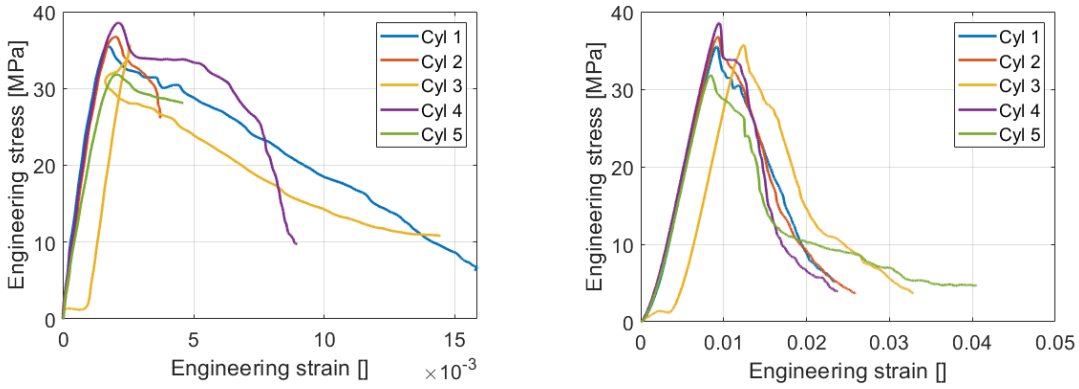

(a) DIC **(b)** Testing rig

Figure 5.13: Engineering stress-strain plots of large cylinder compression tests from DIC measurements (a) and measurements from the loading rig (b).

Viso et al. [44], indicating that larger specimens is more likely to contain a weak spot. Thus the larger specimens could be expected to fail at lower stresses than their smaller counterparts. Furthermore the slenderness of the specimens could affect the results. Decreasing the height-/diameter ratio will cause a transition from a uniaxial to a more complex stress state. A correction factor was used, but it may not account for the full effect of the stress triaxiality. Even accounting for these effects, the strength difference seems to be unusually large. The causes of this are not known, but could be of interest to study in numerical analyses.

Tensile splitting tests

The tensile splitting strength can according to standard NS-EN: 12390-6 [45] be found as:

$$f_{ct,sp} = \frac{2F}{\pi L d} \tag{5.5}$$

where F is the peak force, and L and d are the specimen height and diameter respectively, measured on the fracture plane of the post-tested specimen. The tensile strength from such tests are known to overestimated by 10-15% [35]. Eurocode 2 for design of concrete structures [37] thus allows for adjusting the obtained values to find the axial tensile strength, f_{ct}, by multiplying by a factor of 0.9. Both values are given in table 5.5. The average tensile splitting strength is 6.65 MPa, with a standard deviation of 0.80 MPa, while the corresponding values for the adjusted axial tensile strength is 5.98 MPa and 0.72 MPa. This is somewhat higher than the Eurocode tabulated tensile strength of B75 concrete of 4.5 MPa.

Table 5.5: Results from tensile splitting tests

Cylinder #	Peak force (kN)	Height (mm)	Diameter (mm)	$f_{ct,sp}$ (MPa)	f_{ct} (MPa)
11	37.09	87.7	37.4	7.20	6.48
12	34.18	91.9	36.3	6.52	5.87
13	39.65	90.0	36.5	7.68	6.92
14	33.4 5	89.6	36.3	6.55	5.89
15	27.71	90.8	36.7	5.29	4.76

5.3 Discussion

Material testing was carried out on concrete and steel reinforcement specimens to provide a basis for calibration of the material models.

The average concrete compression strength was determined to be 85.92 MPa for the cubes and 81.99 MPa for the small cylinders. Notably the large cylinders showed a compression strength of 35.62 MPa,less than half of the other specimens. This could in part be explained by the size effect where the observed strength decreases with increasing size. The full reason for the discrepancy is unknown to the author, and it is of interest to study the specimen size effects further in the following numerical studies.

It was of high interest to further assess the capabilites of DIC for concrete material testing, and promising results were obtained in the pre-cracking regime. The analyses allowed for early detection of cracking in the specimen, but were disappointingly unable to produce good strain measurements, especially after cracking occurred. Here the DIC mesh is unable to retain correlation, and the mesh became severely distorted. This unfortunately made the job of validating the material model difficult in the following chapter.

THIS PAGE INTENTIONALLY LEFT BLANK

Chapter 6

Experimental studies of concrete pipes

The experimental work on concrete pipes considered in this thesis was carried out in conjunction with the master thesis of Krone[18]. The thesis considered experiments conducted in 2018, as well as previous experiments from the work of Kristoffersen []. Only the former is presented here. For a more in-depth, detailed description, the reader is referred to the mentioned works.

Additional tests on concrete pipes, including crushing and internal static pressure tests were also planned, but could not be conducted due to time limitations and unforeseen laboratory problems. The tests are thus recommended to be considered in further work on the subject to investigate the material behaviour in different load scenarios.

6.1 Setup

The tests were carried out in collaboration with the Norwegian Defence Estates Agency (NDEA). Concrete pipes with inner diameter of 200 mm and 400 mm were tested. The smaller pipes were plain, while among the larger pipes both plain and reinforced pipes were used.All pipes are mass produced, and any material or geometrical discrepancies between the different pipes should be minimal. 18 pipes were tested in total: 6 plain small pipes, 6 plain large pipes and 6 reinforced large pipes. Geometry of the small and large pipes are illustrated in figures 6.1 and 6.2 respectively. The reinforcement consists of 12 8 mm longitudinal bars, as well as a 6 mm spiral in the circumferential direction, with 100 mm spacing per full rotation.

All pipes were placed on supports of wooden planks and pallets for stability. Spherical charges of C-4 were placed centrally both in the pipe cross-section and along its longitudinal axis. Eight Kistler 603B piezoelectric pressure sensors were used to sample the pressure, at a frequency of 1 MHz. Six of the sensors were placed outside the pipe along its longitudinal axis, at the approximate height of the inner pipe surface. The final two sensors were placed in holes drilled into the pipe wall. In the small pipe they are

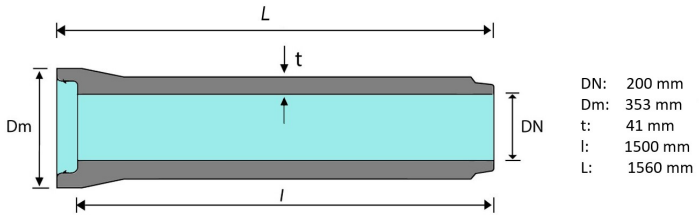

Figure 6.1: Geometry of small pipe

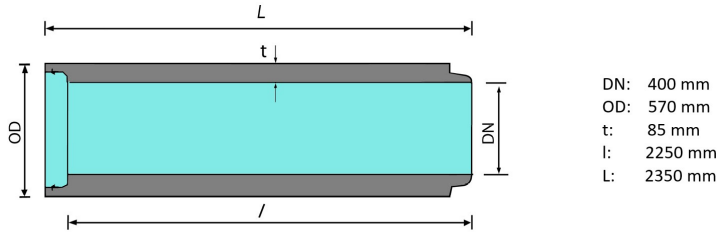

Figure 6.2: Geometry of large pipe

located 10 cm and 20 cm from the pipe opening, while the corresponding distances for the large pipe were 15 cm and 25 cm.

6.2 Results

Table 6.1: Experimental tests on small concrete pipes

Pipe ID	C-4 mass (g)	Z ($m/kg^{1/3}$)	Damage
XVIII	10	0.464	Intact
XIX	12	0.437	Intact
XX	14	0.415	Fragmentation,large oblong pieces
XXI	16	0.397	Fragmentation, large oblong pieces
XXII	18	0.382	Fragmentation,medium size pieces
XVII	20	0.368	Fragmentation, medium size pieces

The small pipes failed at a charge size between 12 and 14 g. In the previous tests carried out in the work of Kristoffersen in 2017 failure was observed at a 13 g charge size. Increasing the charge size beyond this naturally caused more damage, fragmenting the pipe into smaller and smaller pieces.

Table 6.2: Experimental tests on large unreinforced concrete pipes

Pipe ID	C-4 mass (g)	Z ($m/kg^{1/3}$)	Damage
VI	50	0.543	Intact
X	65	0.497	Pipe split in half
VII	75	0.474	Fragmentation, large pieces
VIII	75	0.431	Fragmentation,large pieces
V	100	0.431	Fragmentation, small pieces
I	150	0.376	Fragmentation, small pieces

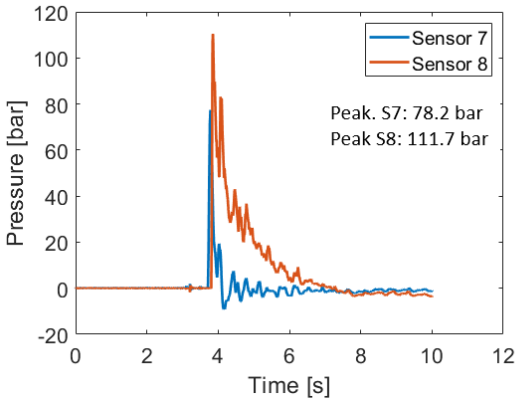

Figure 6.3: Pressure measurements from sensors 7 and 8 in pipe VI

The large pipes failed at a charge size of 65 g, splitting in half along the longitudinal axi At charge sizes of 75 g and above the pipes fragmented into increasingly smaller pieces, as well as scattering the fragments around in a larger area.

Pressure measurements at sensors 7 and 8 for the 50 g C-4 mass (pipe VI) can be seen in figure **??**

The reinforced pipes clearly exhibited a much higher blast resistance than their plain counterparts. The lower charge sizes caused surface cracking and blew off the connecting flanges, but the pipes were otherwise intact. Increasing the charge size caused more severe cracking both on the outside and inside, and at 400 g fragments came loose at the centre of the pipe, exposing the reinforcement steel. The damage and cracking are depicted in figure 6.4 for the pipe with a 500 g charge size.

Table 6.3: Experimental tests on large reinforced concrete pipes

Pipe ID	C-4 mass (g)	Z ($m/kg^{1/3}$)	Damage
II	150	0.376	Small surface cracks
III	200	0.342	Medium surface cracks
IV	300	0.299	Larger cracks
IX	400	0.271	Even larger cracks, rebar exposed
XII	400	0.271	As pipe IX
XI	500	0.252	Severe cracking and fragmentation, rebar exposed

(a) Inside pipe cracking

(b) Cracking on pipe with visible fragmentation in the centre.

Figure 6.4: Damage in pipe subjected to a 500 g C-4 charge.

6.3 Discussion

The small and large plain pipes failed at charge sizes of about 13 g and 65 g C-4, respectively. The addition of reinforcement steel in the large pipes clearly improved the blast resistance, where a charge size of 400 g was required to cause through-thickness cracks and expose the reinforcement steel.

Increasing the charge size generally caused the pipe to fragment into smaller pieces. From the previous work described in the thesis of Krone [18], tests with contact charges showed that confined blasts, as well decreasing the stand-off distance both increased the damage.

Chapter 7

Numerical studies of material tests

Numerical simulations were carried out in the finite element software LS-DYNA to calibrate the concrete material models and assess how well it represents the behaviour observed in the simple experimental tests. Simulations to validate the steel material model could unfortunately not be carried out due to time limitations.

All concrete tests are modelled with two rigid plates. The bottom plate has fixed boundary conditions in all directions, and the top plate is fixed in all directions except the loading direction where it has a prescribed velocity. Interaction between the parts is modelled with surface to surface contact enforced with the penalty method. The friction coefficient between steel and concrete was by Rabbat and Russell [46] observed to vary between 0.57 and 0.7. They recommended using the value of 0.57 for dry contact. Hillestad and Pettersen [17] found that the friction coefficient had to be reduced to one hundreth of this in LS-DYNA to replicate the experimental results. The contact friction coefficients both for static and dynamic friction in the reference model were thus elected as 0.0057.

The duration of the physical experiments were of about 200-300 s, and time-scaling is used to shorten the simulation time to one thousandth of this, i.e 200-300 ms. Furthermore the hourglass control is included as the standard LS-DYNA viscous form, with an hourglass coefficient of 0.1 Energy balance checks are conducted to ensure the kinetic and hourglass energies were sufficiently small. Simulations are run with double precision to avoid inaccuracies as the number of time steps might be substantial. For validation the results are compared to cube 1, and cylinders 4 (large) and 8 (small), as these had the best DIC measurements.

The K&C model allows for full parameter generation based on the sole input of the compressive strength. From the compressive tests this was determined at 85.92 MPa for the concrete cubes, which is used in the reference models for all simulations.

Properties of the reference models for the different tests are summed up in table 7.1.

Test	Element type	Element size
Cube compression	C3D8R*	4mm
Cylinder compression (large)	C3D8R*	5mm
Cylinder compression (small)	C3D8R*	2mm
Splitting tensile	C3D8R*	3mm

* Eight-node linear brick elements with reduced integration.

Table 7.1: Overview of numerical models for concrete tests

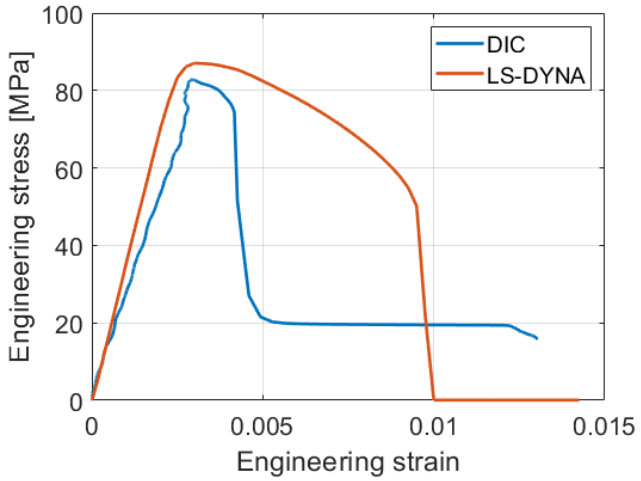

Figure 7.2: Comparison of resulting stress-strain plots from experiments(DIC) and numerical simulations.

7.1 Cube compression tests

The reference model is established with elements of size 4 mm, and is depicted in figure7.1. Resulting engineering stress-strain history is depicted in figure **??** alongside the experimental results.

The simulations does reasonably well in qualitatively capturing the peak stress, but has a slightly higher elastic stiffness modulus than measured in DIC. Furthermore the model is much more ductile than what was seen in the experiment. This might in part be caused by the difficulties in retaining correlation and producing good strain measurements from DIC. Aside from this the model seems to perform reasonably well.

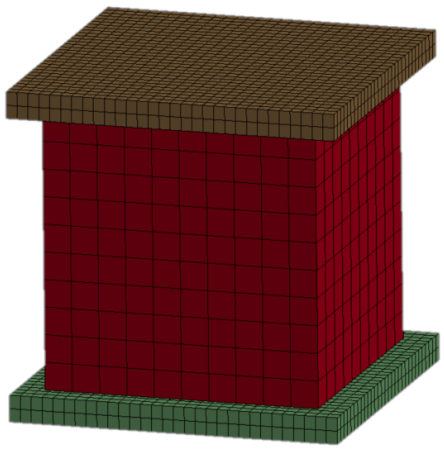

Figure 7.1: Model of cube compression test

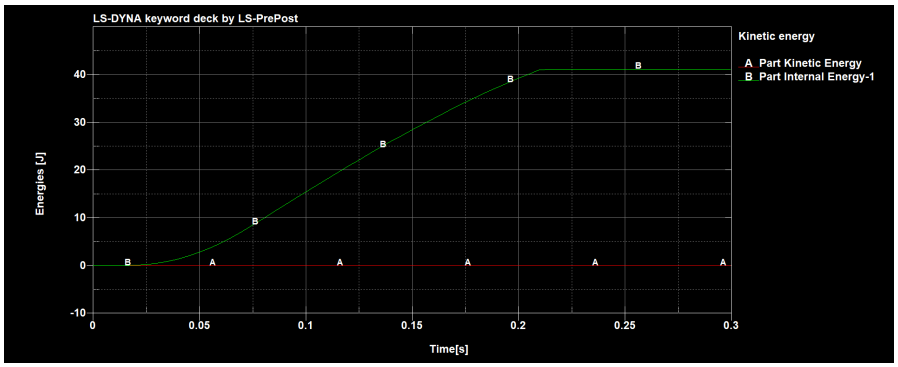

Figure 7.3: Comparison of internal and kintetic energy from numerical simulation of cube compression test.

The kinetic and internal energy quantities in the system are plotted in figure 7.3, and it is clearly seen that dynamic effects are negligible.

7.1.1 Cylindrical compression tests

Simulations with the cylindrical specimens also prduced reasonable results, as seen in figure 7.5. Notably the simulations on large cylinders does not reproduce the surprisingly low strenght observed experimentally, and the compression strength is similar for both cylinder sizes.

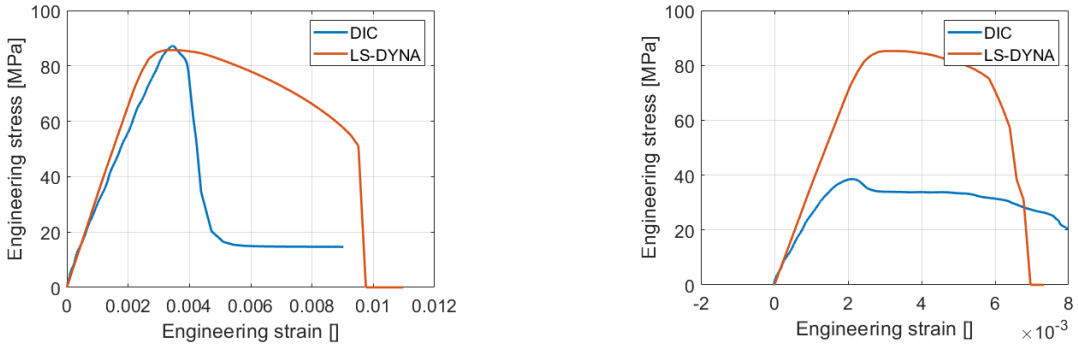

(a) Small cylinders **(b)** Large cylinders

Figure 7.4: Engineering stress-strain plots from experiments and simulations for the small cylinders (a) and large cylinders (b).

7.2 Tensile splitting tests

Simulating the tensile splitting test gave disappointing results, as the force peaked at only around 23 kN early in the simulations, before dropping to zero as the specimen

continued to deform. Force-displacement histories from the experiments and numerical analysis are plotted in figure 7.6. The reason for this is unknown, and was not examined further due to time limitations. Assessing the impact of the tensile strength parameter in the K&C model would also have been of interest. Qualitatively the numerical model did produce a satisfying result with respect to fracture pattern prediction, as illustrated in figure 7.5.

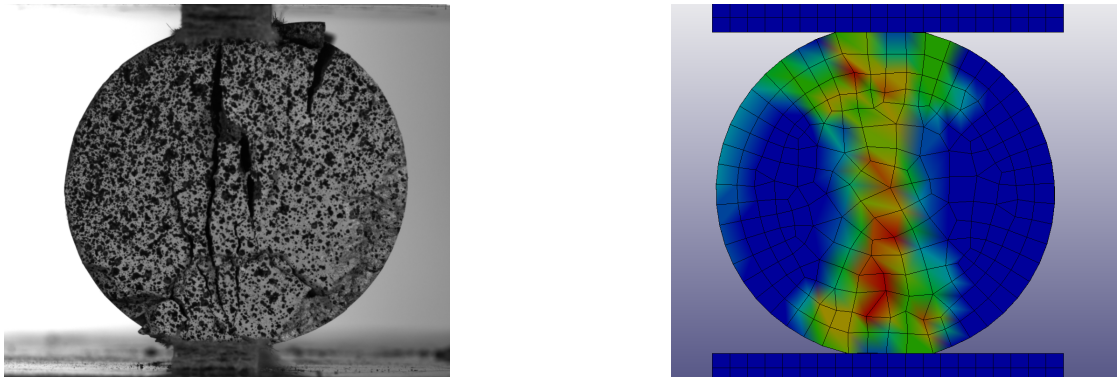

(a) **(b)**

Figure 7.5: Comparison of fracture in experiments on cylinder 15 (a) and plastic strain from numerical simulations

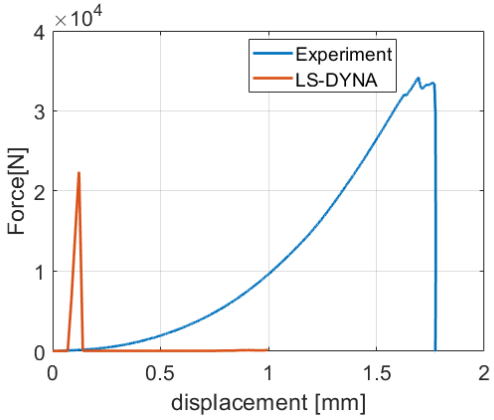

Figure 7.6: Force-displacement relations of experimental tests and simulations in LS-DYNA.

7.2.1 Parameter Study

Parametric studies are conducted with a focus on the cubical specimens to assess the effects of mesh size, friction coefficient, material model compression and tensile strengths, as well as specimen size effects. In the studies all other parameters are kept constant as chosen in the reference model while varying the parameter in question.

Element size

Simulations were run with half and double element size of the reference model, i.e. 2 mm and 8 mm. The three models are shown in figure 7.7. Reducing the element size by half does not affect the result markedly, and the computational costs it brings by increasing the number of elements from 1000 to 8000 does not seem to warrant the extra accuracy.

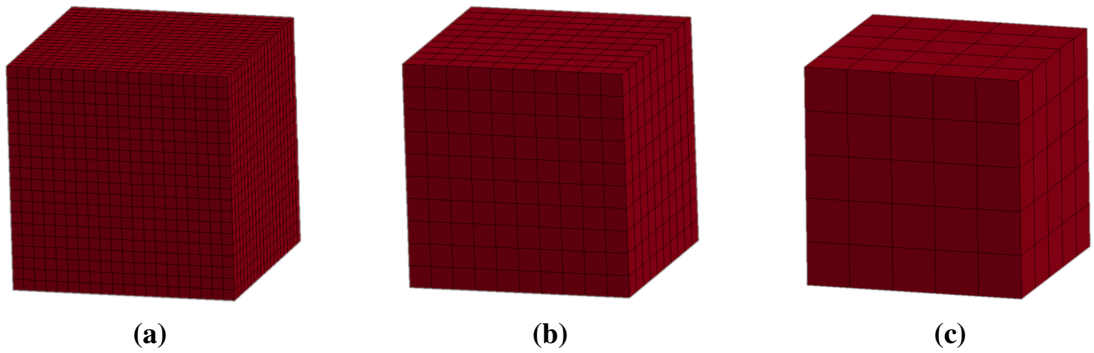

(a) **(b)** **(c)**

Figure 7.7: Models with elements sizes of 2 (a), 4 (b), and 8 (c) mm.

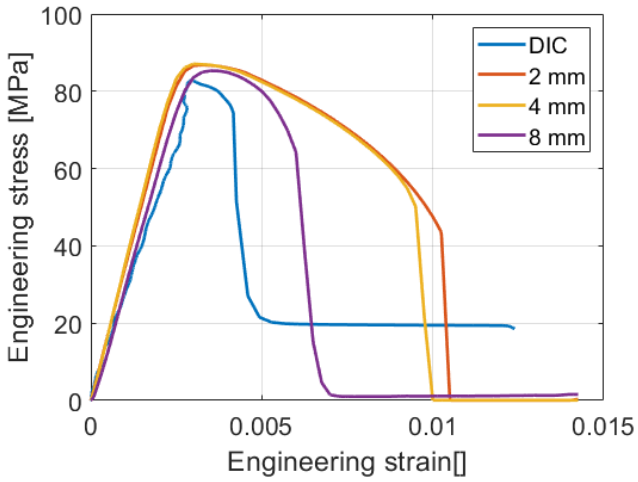

Figure 7.8: Stress-strain plot with different element sizes

Friction Coefficient

The preceding master theses on the same subject observed that the friction coefficient was a highly influential parameter for the numerical material studies in LS-DYNA. As such they were also chosen for assessment here. Other than the reference coefficient of 0.0057, simulations were run with parameter values of 0.057 and 0.57, which is the real friction coefficient between concrete and steel. It is seen that nonphysically low parameter values are needed to approach the experimental results. Using the theoretical value of 0.57 produces the worst result, almost doubling the capacity of the cube,

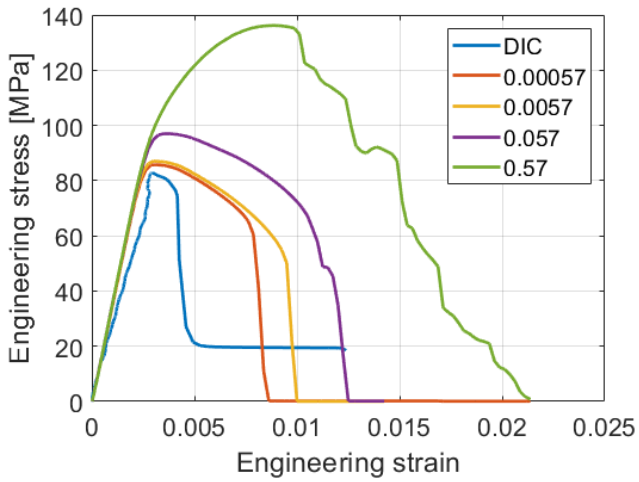

Figure 7.9: Stress-strain plot with various friction coefficients

Compression and tensile strengths

The compression strengths used in the K&C concrete material model for parameter generation is studied to see how it affects the behaviour in the compression tests. Other than the reference compression strength of 85.92 MPa, simulations are also run with strengths of 75 MPa and 95 MPa.

Furthermore the uniaxial tensile strength may be added as a parameter in the material model. Simulations were run with the parameter set as the experimentally found axial tensile strength of 5.98 MPa, as well as with an intermediate value of 3.5 MPa.

Altering the compression strength seems to quantitatively scale the stress-strain curve, without changing the shape and qualitative behaviour. To capture the peak stress from the experiments it is seen that the compression strength should be around 80 MPa: smaller than the experimentally observed value.

Having no tensile strength input nearly coincides exactly with a parameter value as the experimentally found tensile strength, indicating that the parameter generation of the K&C model corresponds very well with the experimental work. Lowering the strength to 3.5 MPa clearly lowers the models material capacity with respect to ductility, but the peak stress remains unchanged as it is dependent on the input of compression strength. The lowered tensile strength input of 3.5 MPa is closer to the DIC-curve, but calibrating

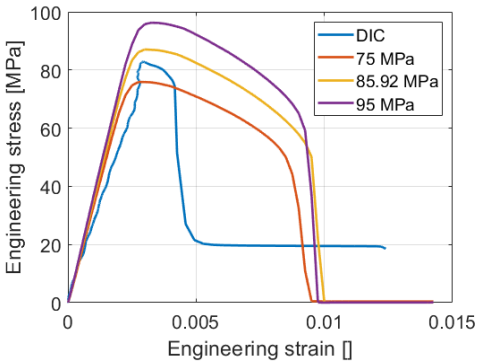

(a) Compression strength parameter study

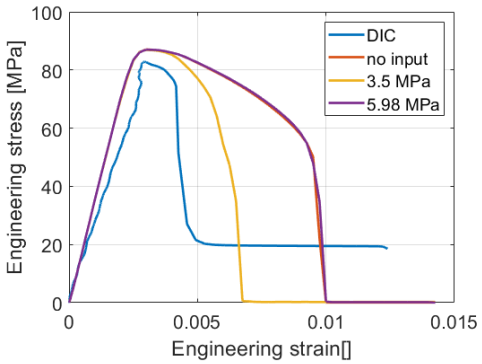

(b) Tensile strength parameter study

Figure 7.10: Stress-strain plots for different compression strengths (a), and tensile strengths (b).

the material model accordingly is not done due to the uncertainties in connected to the DIC analyses.

7.3 Discussion

The numerical simulations overall seem to perform well, but the material model is hard to validate due to the problems with DIC measurements. The frictional coefficient is observed to be highly influential on the specimen capacity, and unrealistically low values are required to approach the experimental results. Element sizes of 4 mm appears to be a reasonable choice for modelling the concrete cubes, and offers a good compromise between accuracy and computational efficiency. While the parameter generation of K&C model works well, tuning the other material parameters, such as tensile strength, seems useful in improving its performance, and warrants further study.

THIS PAGE INTENTIONALLY LEFT BLANK

Chapter 8

Numerical studies of concrete pipes

Numerical studies of the concret pipes were performed using FE code LS-DYNA with the purpose of assessing the performance of the K&C material model under blast loading as well as the capability of the ConWep model to recreate blast loading in confined environments.

Ideally the elements would be of identical size as the elements used to calibrate the material model in the compression simulations. The size of the pipe made this impossible, and the element size was increased to 50 mm to avoid excessive computation costs.

The blast load is simulated with the ConWep model and *BLAST ENHANCED keyword in LS-DYNA, and is applied to affect the inner surface of the tube.

8.1 Blast load replication

An initial reference model using Lagrangian simulations was made to observe how the ConWep model is able to replicate the measured pressure loading from the experiments. The ConWep model is based on empirical data from free-field explosions, of which a limited amount hsa scaled distances Zlower than 0.4. The effects of a the close-in blast and confinement of the pipe is thus not accounted for in the model, and it was of great interest to observe the discrepancy in the pressure measurements between the two. For comparison the experiment of a large pipe with a 50 g centrical charge size was chosen. This choice was made with the goal of simplifying the model, as little damage was observed in this test, thus allowing for a simpler model where the produced pressures are not significantly affected by deformation of the pipe. As the structural response was not in focus, the pipe is modelled as rigid. Initial simulations with the *Mat_rigid keyword would not produce any pressure readings. It was decided to model the pipe using the *Mat_elastic keyword with steel parameters, which should produce a behaviour stiff enough to be considered rigid.

The experimental studies measured interior pressure in the pipe in two pressure sensors

in the pipe wall at distances 10 and 15 cm from the narrow end. Pressure measurements in the simulations were extracted from elements at the same locations for comparison.

8.1.1 Results

Blast load simulations caused a resultant displacement of 0.1 mm for a charge size of 5 kg, and is substantially smaller for all charge sizes closer to the actual explosive mass from the experiments. Assumptions of a rigid pipe are thus reasonable.

In figure 8.1 the pressure measurements from sensors 7 and 8 in the experiment are compared to pressure readings at the same locations in the numerical model. Measurements at sensors 7 and 8 are roughly 100 times larger in the experiment than in the simulations, and even the pressure in the middle of the pipe only reaches half of the empirical pressure peak. Additionally it is observed that the pressure wave arrives earlier in the simulations. T

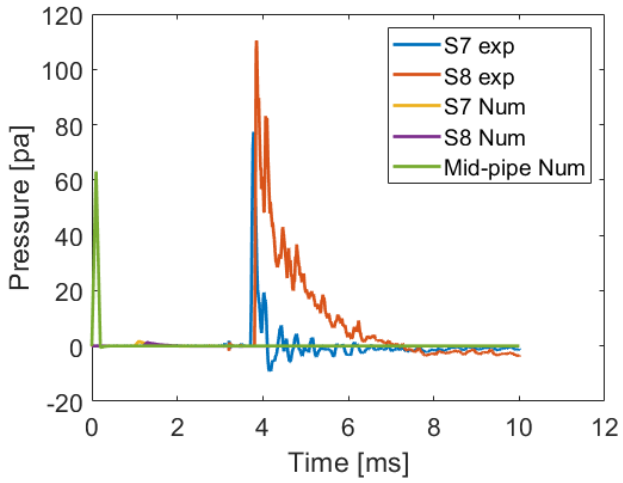

Figure 8.1: Pressure comparison of experiment and numerical simulation

In an attempt to approach the experimental pressure magnitudes, a parametric study is conducted with varying charge sizes. Simulations are run with explosive masses of 0.1 kg, 0.5 kg, 1.0 kg and 5.0 kg. Resulting pressure measurements in the simulations shown in figure 8.2 are still greatly underestimating the pressures even for charge sizes 100 times larger than in the experiments. Furthermore, increasing the charge size seems to speed up the shock wave, shortening its arrival time at the sensors.

8.2 Simulations on structural response

While the ConWep model greatly underestimate the pressures, it is further applied to examine how the K&C concrete model is able to predict the behaviour of the concrete. A new model is thus established where the K&C model is used in place of the previous

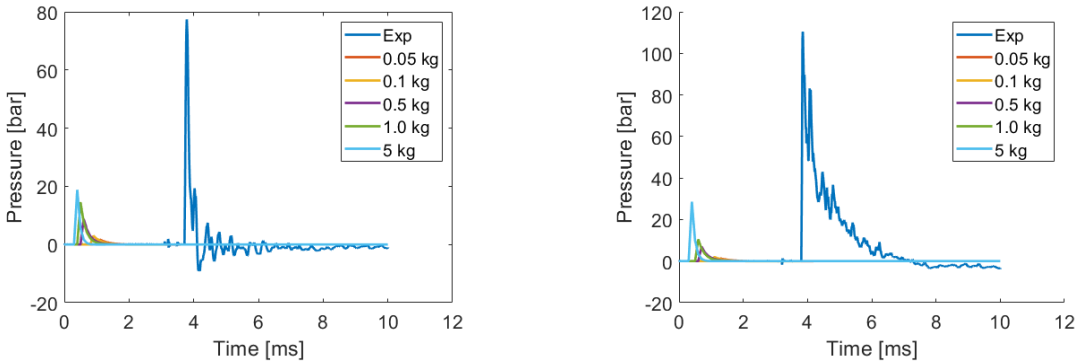

(a) Sensor 7 **(b)** Sensor 8

Figure 8.2: Pressures from parameter study with charge sizes

elastic material model with steel parameters (assumed rigid). Due to time limitations the element size is still kept as 50mm, thus only offering a rough approximation of the pipe response. A charge size of 50g is applied in the ConWep model.

8.2.1 Results

The damage evolution over time is shown in figure 8.3. The pipe damage is clearly significant, and larger than in the experiments where the pipe was intact, even though ConWep underestimates the pressures. The damage is concentrated in the middle section of the pipe, and some longitudinal cracks are seen propagating towards the pipe openings.

Finally the charge size was upped to 100g to observe how this would affect the damage in the pipe. Figure 8.4 depicts the effective plastic strain in the pipe at a time 10 ms after detonation. Comparatively to a charge size of 50g the pipe is seen to experience more damage in the central section, while the extent of cracking towards to pipe openings has reduced.

8.3 Discussion

The ConWep blast loading model is seen to underestimate the pressures greatly for internal blasts, and is thus non-conservative for such scenarios. It should be noted that the study conducted here has been limited due to time constraints, and spending more time developing and tuning the model could have significant effects in adjusting the ConWep model to produce viable results. For example studying the effect of mesh size would clarify if the coarse mesh applied had any effect on the ConWep model underestimating pressures, although this seems unlikely to have such a significant effect.

Part of the reason for the large discrepancy between pressures lies with the effects of confinement and afterburn. Confinement causes amplification of the pressures as the

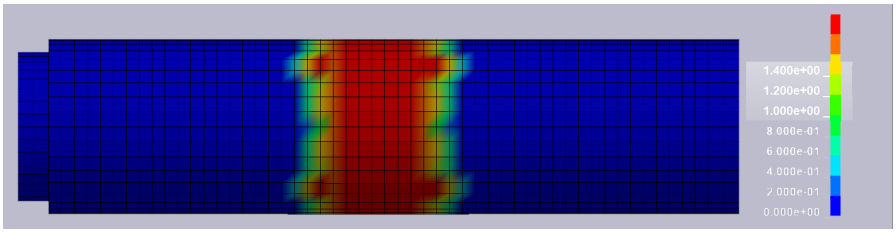

(a) 0.2 ms

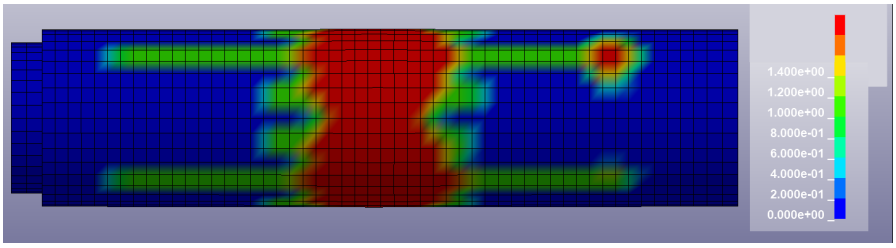

(b) 1 ms

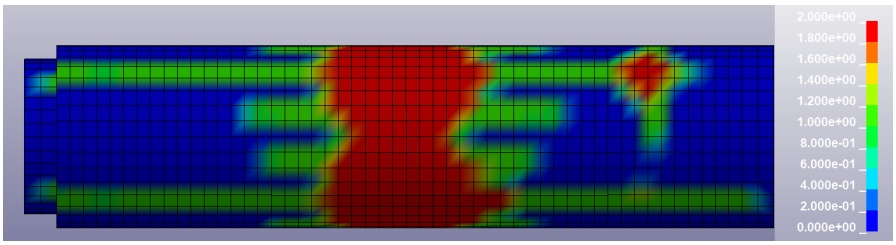

(c) 10 ms

Figure 8.3: Damage evolution over time visualised by the effective plastic strain.

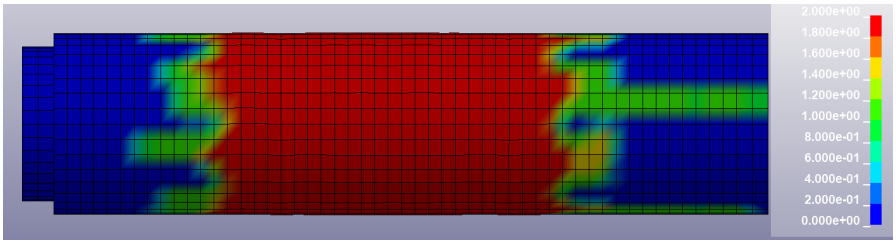

Figure 8.4: Damage in simulations of pipe with a 100 g charge size

shock waves bounce back and forth. Afterburn may also contribute with significant energy in the tubular pipe experiments where the detonation products are unable to vent. The JWL-EOS in LS-DYNA has an option that allows for adding extra energy over time to simulate the effect of afterburn. Exploring this option to see if it could improve blast load prediction in confined environments could prove enlightening.

The K&C model seems to overestimate the damage even though ConWep predicts a pressure loading significantly smaller than seen in the experiments. Qualitatively the damage prediction is reasonable however, predicting the largest damage in the centre, with long cracks propagating in the longitudinal direction. The model could probably be improved through further development and validation of the material model. Adding erosion criteria could improve the response, and in particular offer better visualisation of the damage.

All in all the K&C model seems promising, but requiring of further work and tuning than what there was time for in this thesis.

THIS PAGE INTENTIONALLY LEFT BLANK

Chapter 9

Concluding Remarks

The experimental studies of material tests provided an extensive and valuable basis of comparison for numerical simulations to assess the performance of the material models. Digital image correlation (DIC) is a useful tool in obtaining good deformation measurements. However, obtaining correct measurements for a material with brittle tendencies, such as concrete, caused some problems, and the deformation after cracking occurred was only captured to come extent. Further tuning of the analysis, including multiscaling over frames where correlation is lost could improve the results. The analyses still performed satisfyingly in the pre-cracking domain, and the earlier results of Skaare [19] and Krone [18] warrants further use of DIC also for testing of concrete. The concrete strength observed in the experiments notably was halved for the large cylindrical specimens. The reason for this is unknown to the author, and could unfortunately not be studied further due to time limitations.

Finite element software LS-DYNA provides numerous concrete material models, and the Karagozian and Case model was used to simulate the behaviour of the concrete. Based on a simple input the model gave decent results, however validation against experimental work offered some problems due to the limited accuracy obtained through DIC-analyses. A parameter study on compression strength and tensile strength indicated that tuning of the material model could improve its performance further. Mesh size naturally affects the results, but the element size of 4 mm in the reference model seemed to offer a good compromise between accuracy and computational efficiency. The friction coefficient had to be unphysically small (0.0057) to replicate the experimental results, and using the experimentally found value of 0.57 greatly overestimates the specimen capacities.

Static inner pressure tests using water pressure as well as crushing tests were planned performed on concrete pipes, but had to be postponed due to unforeseen problems at the laboratory. As an experimental basis, the previously conducted work in conjunction with the thesis of Krone [18] was used.

The numerical studies on concrete pipes showed that the ConWep model is simple to

use, but is unable to predict the blast loading accurately for confined explosions. This seems natural, as it is based on the empirical date of Kingery and Bulmash, where the experiments were free-air explosions of hemispherical surface burst.

The fact that the pipe damage still is overestimated corresponds with what has been observed in the previous master theses [18], and seems to indicate that the K&C concrete model is unable to accurately predict the structural response for such complex load scenarios. Further tuning and validation of the model might work to remedy this. The qualitative damage prediction was nevertheless promising, and warrants further study.

In conclusion, the internal blast load is a complex scenario that the models used in this thesis was unable to accurately capture. Unfortunately the work put into this thesis came up short in order to achieve this.

9.1 Further Work

Experimental studies on reinforcement steel has been presented briefly, but a thorough validation of a steel material model based on both quasi-static and dynamic (SHTB) was left out in favour of other areas of work. Establishing the material model by numerical simulations of the material tests is expected to be valuable before eventually applying it in numerical simulations of the blast experiments with reinforced pipes.

The planned tests on the concrete pipes (static pressure and crushing) could provide further understanding of the concrete behaviour under various loads, as well as validation bases for material models, and should be of interest in future work.

Eulerian simulations to better predict the blast pressures, as well as coupled Eulerian-lagrangian analyses, possibly including FSI effects are also possible avenues to pursue in forthcoming studies on the subject.

Other points of interest in future work are studying further how well other concrete material models perform, including stochastic models such as the ones used by Hillestad and Pettersen [17] and Krone [18]. Inclusion of erosion-criteria in concrete material model, studying other finite element codes, and in particular conducting simulations using particle models are other interesting possibilities in future work.

Eventually a goal of these studies is naturally numerical simulations on full SFT cross-sections, but on the basis of this thesis it seems far-fetched before a more thorough validation and adjustment of both material models and blast load prediction models are carried out.

Bibliography

[1] Norwegian Public Roads Administration. The E39 Coastal Highway Route. https://www.vegvesen.no/vegprosjekter/ferjefriE39, 2018. Accessed: 01.10.2018.

[2] Norwegian Public Roads Administration. "Mulighetsstudie for kryssing av Sognefjorden - Neddykket rørbru " [Feasibility study for crossing the Sognefjord - Submerged floating tunnel]. https://www.vegvesen.no/_attachment/513902/binary/828560, 2018. Accessed: 01.10.2018.

[3] M. Foglar and M. Kovar. Conclusions from experimental testing of blast resistance of FRC and RC bridge decks. *International journal of Impact Engineering*, 59:18–28, 2013.

[4] and S. Mishra R.K. Chaudhary, T. Chakraborty, and V. Matsagar. Vulnerability analysis of tunnel linings under blast loading. *International Journal of Protective Structures*, 96:1–22, aug 2018.

[5] R. Tiwari, T. Chakraborty, and V. Matsagar. Analysis of curved tunnels in soil subjected to internal blast loading. *Acta Geotechnica*, 96:1–2, 2018.

[6] Y. Li, O. Algassem, and H. Aoude. Response of high-strength concrete beams under shick-tube induced blast loading. *Construcion and Building Materials*, 189:420–437, 2018.

[7] B. Luccioni, F. Isla, R. Codina, D. Ambrosini, R. Zerbino, G. Giaccio, and M.C. Torrijos. Experimental and Numerical Analysis of Blast Response of High Strength Fiber Reinforced Concrete Slabs. *Engineering Structures*, 175:113–122, 2018.

[8] G.K. Park, H.G Kwak, and F.C Filippou. Evolution of nonlinear behavior and resisting capacity of reinforced concrete columns subjected to blast loads. *Engineering Failure Analysis*, 93, 2018.

[9] L. Javier Malwar, John E. Crawford, James W. Wesevich, and Don Simons. A plasticity concrete material model for DYNA3D. *International Journal of Impact Engineering*, 19:847–873, 1997.

[10] W. Guo, W. Fan, X. Shao, D. Shen, and B. Chen. Constitutive model of ultra-high-performance fiber-reinforced concrete for low-velocity impact simulations. *Composite Structures*, 185:307–326, 2018.

[11] J. Wu, L. Li, X. D, and X. Lie. Numerical study on the asphalt concrete structure for blast and impact load using the Karagozian and Case concrete model. *Applied Sciences*, 7, 2017.

[12] M. Kristoffersen, A. Minoretti, and T. Børvik. On the internal blast loading of submerged oating tunnels in concrete with circular and rectangular cross-sections. 6, 2019.

[13] M. Kristoffersen, K.O. Hauge, G. Valsamos, and T. Børvik. Blast loading of concrete pipes using spherical centrically placed c-4 charges. In *International Conference on the Mechanical and Physical Behaviour of Materials under Dynamic Loading, DYMAT 2018*, Archachon, FR, Sept 2018.

[14] M. Kristoffersen and T. Børvik. Blast loading of concrete pipes using c-4 charges†. In *International Conference on Experimental Mechanics (ICEM18)*, Brussels, BE, July 2018.

[15] M. Kristoffersen, A. Minoretti, and T. Børvik. Submerged floating tunnels subjected to internal blast loading. In *Proceedings of 7th Transport Research Arena TRA 2018*, Vienna, AT, April 2018.

[16] S. R. Haug and K. Osnes. Submerged floating tunnels subjected to internal blast loading. Master's thesis, Norwegian University of Science and Technology, 2016.

[17] E. Hillestad and J. E. Pettersen. Experimental and numerical studies of plain and reinforced concrete plates subjected to blast loading. Master's thesis, Norwegian University of Science and Technology, 2016.

[18] E. Krone. Internal blast loading of submerged floating tunnels in concrete. Master's thesis, Norwegian University of Science and Technology, 2018.

[19] N. K Skaare. Submerged floating tunnels exposed to internal blast loading. Master's thesis, Norwegian University of Science and Technology, 2018.

[20] T. Jankowiak and T. Lodygowski. Identification of parameters of Concrete Damage Plasticity constituitive model. *Foundations of civil and environmental engineering*, 6:53–69, 2005.

[21] V. Aune, T. Børvik, and M. Langseth. Lecure Notes in TKT4128 Impact Mechanics: An Introduction to Blast Mechanics, 2016.

[22] T. Krauthammer. *Modern Protective Structures*. CRC Press, an imprint of Taylor & Francis Group, Florida, USA, 2008.

[23] Wikipedia contributors. Supersonic speed. https://en.wikipedia.org/wiki/Supersonic_speed. accessed: 06.10.2018.

[24] D. Cormie, G. Mays, and P. Smith. *Blast Effects on Buildings*. Thomas Telford Ltd., London, UK, 2009.

[25] B. Hopkinson. British ordnance board minutes. Report 13565, British Ordnance Office, London, UK, 1915.

[26] C. Cranz. *Lehrbuch der Ballistik*. Springer-Verlag, Berlin, DE, 1926.

[27] S. Courtiaud, N. Lecysyn, G. Damamme, T. Poinsot, and L. Selle. Analysis of mixing in high-explosive fireballs using small-scale pressurised spheres. *Shock Waves*, 29:339–353, 2018.

[28] K. Balakrishnan, F. Genin, D.V. Nance, and S. Menon. Numerical study of blast characteristics from detonation of homogeneous explosives. *Shock Waves*, 20:147–162, 2010.

[29] Eurocode 1: Actions on structures - Part 1-7: General actions - Accidental actions. Eurocode, Standard Norge, Oslo, NO, 2008.

[30] C.N. Kingery and G. Bulmash. *"Airblast Parameteres from TNT Spherical Air Burst and Hemispherical Surface Burst"*. Defence Technical Information Center, Ballistic Research Laboratory, Aberdeen Proving Ground, Maryland, USA, 1984.

[31] Wikipedia contributors. Ideal gas law. https://en.wikipedia.org/wiki/Ideal_gas_law. accessed: 15.01.2019.

[32] W.E Baker, P.A Cox, J.J Kulesz, R.A Strehlow, and P.S Westine. *Explosion Hazards and Evaluation*. Elsevier, Amsterdam, 1983.

[33] Folco Casadei, Martin Larcher, and Nicolas Leconte. Strong and Weak Forms of a Fully Nonconforming FSI Algorithm in Fast Transient Dynamics for Blast Loading of Structures. In *COMPDYN 2011 Proceedings of the 3rd Int. Conference on Computational Methods in Structural Dynamics and Earthquake Engineering*, pages 1120–1139, 2012.

[34] O.S. Hopperstad and T. Børvik. Lecure Notes in TKT4128 Impact Mechanics: Modelling of Plasticity and Failure with Explicit Finite Element Methods, 2017.

[35] P. K. Mehta and P.J. M. Monteiro. *Concrete: Microstructure, Properties, and Materials, 3rd ed.* McGraw-Hill Companies, 2005.

[36] J.P. Ollivier, J.C. Maso, and B. Bourdette. Interfacial transition zone in concrete. *Advanced Cement Based Materials*, 2:30–38, 1995.

[37] Eurocode 2: Design of concrete structure - Part 1-1: General rules and rules for buildings. Eurocode, Standard Norge, Oslo, NO, 2018.

[38] J. Ožbolt, A.Sharma, B. İrhan, and E. Sola. Tensile behaviour of concrete under high loading rates. *International Journal of Impact Engineering*, 69:55–68, 2014.

[39] J.M. Magellanes, Y. Wu, L.J. Malwar, and J.E. Crawford. Recent improvements to release iii of the kc concrete model. In *International LS-DYNA User Conference*, June 2010.

[40] G. R. Johnson and W. H. Cook. A constitutive model and data for metals subjected to large strains, high strain rates and high temperatures. In *7th Int. Symposium on Ballistics*, pages 541–547, aug 1983.

[41] M.G. Cockroft and D.J. Latham. Ductility and the workability of metals. *Journal of the Institute of Metals*, 96:33–39, 1968.

[42] NS-EN 12390-1: Testing hardened concrete - Part 1: Shape, dimensions an other requirements for specimens and moulds. Eurocode, Standard Norge, Oslo, NO, 2012.

[43] "Byggforsk 520.033 : Bestemmelse av betongkonstruksjoners trykkfasthet. Uttak og prøving av sylindre". Byggforsk, SINTEF Byggforsk, Trondheim, NO, 2013.

[44] J.R del Viso, J.R Carmona, and G. Ruiz. Shape and size effects on the compressive strength of high-strength concrete. *Cement and Concrete Research*, 38:386–395, 2008.

[45] NS-EN 12390-1: Testing hardened concrete - Part 6: Tensile splitting strength of test specimens. Eurocode, Standard Norge, Oslo, NO, 2009.

[46] B.G. Rabbat and G. Russell. Friction Coefficient of Steel on Concrete or Grout. *Journal of Structural Engineering*, 111:61–81, 1985.

Appendix A

Theory

A.1 Blast Loading

D.3 Explosions in road and rail tunnels

(1) In case of a detonation in road and rail tunnels, the pressure time function may be determined using expressions (D.7) to (D.9), see Figure D.1(a):

$$p(x,t) = p_0 \exp\left\{-\left(t - \frac{|x|}{c_1}\right)/t_0\right\} \text{ for } \frac{|x|}{c_1} \le t \le \frac{|x|}{c_2} - \frac{|x|}{c_1} \quad \text{(D.7)}$$

$$p(x,t) = p_0 \exp\left\{-\left(\frac{|x|}{c_2} - 2\frac{|x|}{c_1}\right)/t_0\right\} \text{ for } \frac{|x|}{c_2} - \frac{|x|}{c_1} \le t \le \frac{|x|}{c_2} \quad \text{(D.8)}$$

$$p(x,t) = 0 \text{ for all other conditions} \quad \text{(D.9)}$$

where:

p_0 is the peak pressure (=2 000 kN/m^2 for a typical liquefied natural gas fuel;

C_1 is the propagation velocity of the shock wave (~ 1 800 m/s);

C_2 is the acoustic propagation velocity in hot gasses (~ 800 m/s);

t_0 is the time constant (= 0,01 s);

$|x|$ is the distance to the heart of the explosion;

t is the time.

(2) In case of a deflagration in road and rail tunnels, the following pressure time characteristic may be taken into account, see Figure D1(b):

$$p(t) = 4p_0 \frac{t}{t_0}\left(1 - \frac{t}{t_0}\right) \text{ for } 0 \le t \le t_0 \quad \text{(D.10)}$$

where :

p_0 is the peak pressure (=100 kN/m^2 for a typical liquefied natural gas fuel;;

t_0 is the time constant (= 0,1 s);

t is the time.

(3) The pressure determined by expression (D.10) may be used for the entire interior surface of the tunnel.

Figure A.1: Eurocode 1-7 entry on calculating pressure history in rail and road tunnels from internal explosions. *Adapted from Eurocode 1*$_{17}$[*29*]

THIS PAGE INTENTIONALLY LEFT BLANK

Appendix B

Experimental Results

Table B.1: Measurements of concrete cylinders for compression tests

Cylinder #	Diameter (mm)	Height (mm)	Weight (g)
1	59.20	93.54	618.4
2	59.22	92.78	616.9
3	59.22	91.41	623.9
4	59.19	92.36	621.0
5	59.20	93.37	621.1
6	32.75	41.22	85.9
7	32.82	41.12	85.6
8	32.80	41.46	85.6
9	32.80	41.92	87.0
10	32.81	41.17	85.7

Table B.2: Measurements of concrete cylinders for compression tests

Cylinder #	Diameter (mm)	Height (mm)	Weight (g)
11	37.40	87.67	235.0
12	37.17	91.53	238.6
13	37.48	89.56	239.9
14	37.39	89.16	237.0
15	37.14	90.19	237.5

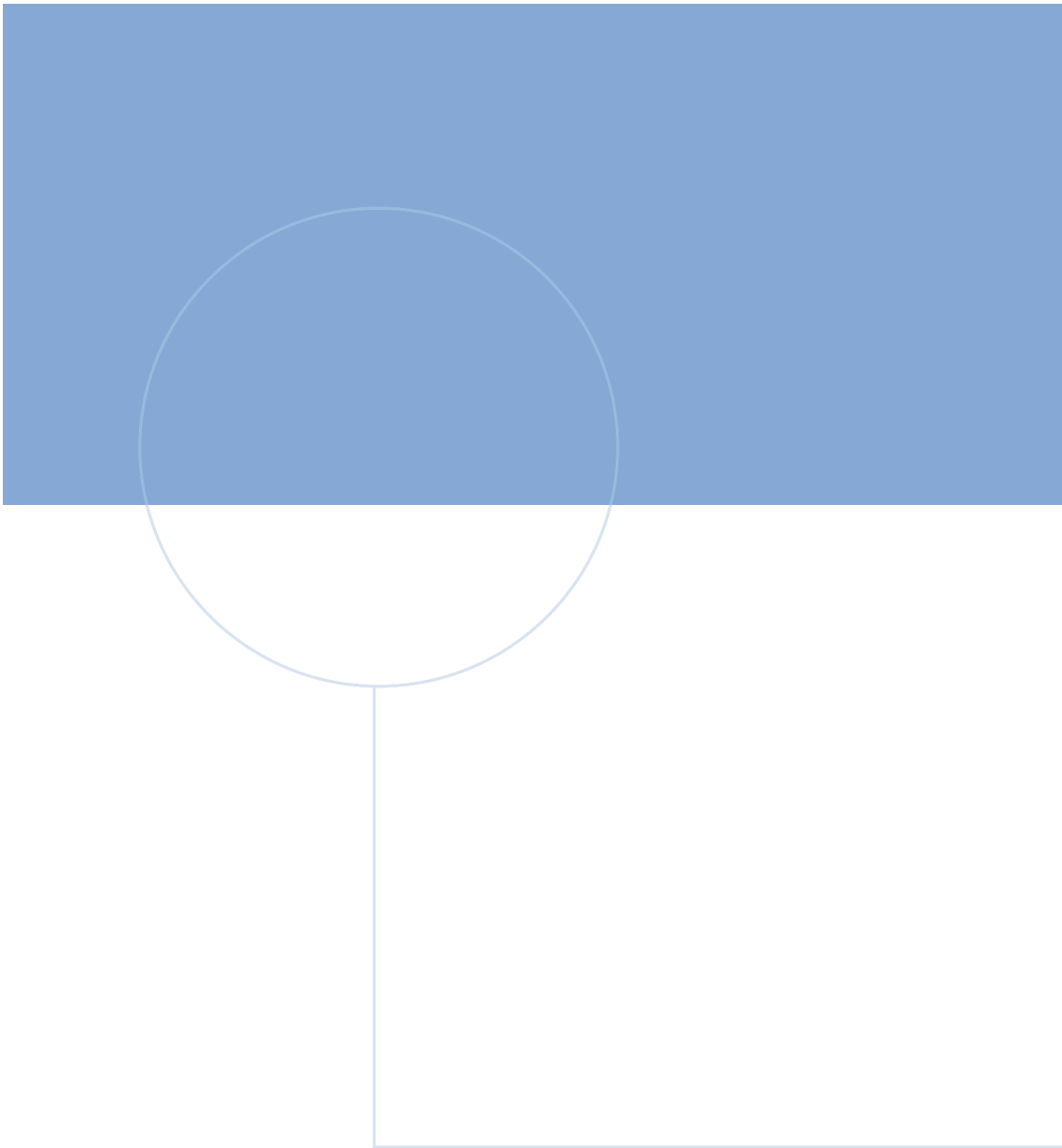

NTNU
Norwegian University of
Science and Technology